

# Basement geology and its controls on the nucleation and growth of rift faults in the northern Campos Basin, offshore Brazil

Michael Strugale<sup>1,2</sup>  | Renata da Silva Schmitt<sup>3</sup>  | Joe Cartwright<sup>2</sup> 

<sup>1</sup>Petrobras S.A., Rio de Janeiro, Brazil

<sup>2</sup>Department of Earth Sciences, University of Oxford, Oxford, UK

<sup>3</sup>Departamento de Geologia - IGEO, Universidade Federal do Rio de Janeiro (UFRJ), Rio de Janeiro, Brazil

## Correspondence

Michael Strugale, Petrobras S.A. Av. Henrique Valadares, 28 - Centro, Rio de Janeiro - RJ, 20231-030, Brazil.  
Email: michael\_strugale@petrobras.com.br

## Funding information

Petrobras

## Abstract

The rift phase of the Campos Basin developed during the Early Cretaceous on a heterogeneous crust comprising structures inherited from the Brasiliano-Pan African tectonic events, mostly generated during the Neoproterozoic-Cambrian amalgamation of western Gondwana blocks. The main rifting episode took place from the Hauterivian to the Barremian, then was succeeded by the transition and post-rift (SAG) phases during the Aptian. Rift faults developed as a result of a progressive rotation of extension from E-W to NW-SE. The role of pre-existing intra-basement structures on the style and evolution of the rift faults was investigated using 3D high-resolution seismic data, borehole logs and sidewall samples. Three seismic facies (SF1, SF2 and SF3) and three types of intra-basement structures (Surfaces, Geobodies and Internal Reflections) were identified and mapped. They represent, respectively, contrasting levels of seismic anisotropy, interpreted as metamorphic foliation, and ductile shear zones that bound rock units with particular seismic facies signatures. Sidewall cores show that banded biotite-gneiss is the predominant rock type in the eastern half of the study area, while more homogeneous granitoid is the dominant lithology on the west. Such a binary division of lithotypes is consistent with the distribution of mapped intra-basement seismic facies and features. The contrasting basement heterogeneity across the study area is the major control in the strain distribution during rifting. Where the basement is highly heterogeneous, the pre-existing fabric was selectively reactivated whenever its orientation was favourable, resulting in faults forming progressively as the extension direction rotates, whilst shallower low to very low angle basement fabric were cross-cut by rift faults. Where the basement is homogeneous, only early formed faults remain active throughout the rifting.

## KEYWORDS

3D seismic, basement inheritance, brittle reactivation, Campos Basin, Early Cretaceous, rift faults

This is an open access article under the terms of the Creative Commons Attribution License, which permits use, distribution and reproduction in any medium, provided the original work is properly cited.

© 2021 The Authors. *Basin Research* published by International Association of Sedimentologists and European Association of Geoscientists and Engineers and John Wiley & Sons Ltd.

# 1 | INTRODUCTION

The influence of basement fabric on the structural styles of rift basins based on surface geology and remote sensing has been widely reported in the literature (e.g. Daly et al., 1989; Milani & Davison, 1988). Following the advancement in seismic acquisition and processing in the last 20 years, some authors have used 2D and 3D seismic data to interpret basement heterogeneities, both onshore and offshore. Identifying and mapping basement heterogeneities underneath rift basins using 2D seismic (Bird et al., 2014; Fazlikhani et al., 2017; Morley et al., 2004; Phillips et al., 2016; Withjack et al., 1998) and more recently 3D seismic data (Collanega et al., 2019; Lenhart et al., 2019; Osagiede et al., 2020; Reeve et al., 2014) has revealed close relationships between inherited basement structural anisotropy and the structural style of rifting, agreeing with observations made onshore. However, the geometry and composition of the crystalline basement are still largely neglected or simply considered homogeneous in analogue, numeric and tectonostratigraphic models of rift development (Lenhart et al., 2019).

Studies of the Eo-Cretaceous Pre-Salt interval of Campos Basin have thus far been focused on petrography, diagenetic history and depositional environments of reservoir rocks (Dias et al., 1988; Herlinger et al., 2017; Lima & De Ros, 2019; Lima et al., 2020; Mizuno et al., 2018; Muniz & Bosence, 2015; Olivito & Souza, 2020). However, only regional scale research into the Precambrian basement and rift structural geology of the basin has been undertaken (Chang et al., 1992; Fetter, 2009; Guardado et al., 1989; Stanton et al., 2019), along with that the basement rocks of Campos Basin have been considered mostly homogeneous in both regional (e.g. Guardado et al., 1989) and local studies (e.g. Lima et al., 2020). Also, the structures that evolved during the rift initiation and climax are still poorly understood at reservoir scale in the north of the Campos Basin. Finally, correlation of Precambrian units between South America and Africa in the position of the Campos Basin still leads to many open questions, due to the lack of physical continuity and contrasting tectonic and lithological contents between them. In addition, a significant part of the continental crust is submerged under the shelves of South America and Africa (Heilbron et al., 2008; Schmitt et al., 2008, 2016).

We interpreted a 3D high-resolution seismic survey and wellbore data (logs and sidewall cores) to examine the lithological content, structural framework and U-Pb age of the basement. From these data, we explored the relationships between basement heterogeneity and the nucleation, growth, and structural style of the rift faults. Although intra-basement reflectivity has been observed on many deep seismic profiles and from many crustal settings (e.g. Stanton et al., 2019; Withjack et al., 1998), there are few studies that attempt to interpret these reflections systematically (e.g. Fazlikhani et al., 2017; Phillips et al., 2016). In this paper, we map variations in basement structure based on detailed interpretation

## Highlights

- 3D seismic and well interpretation of basement geology and rift faults in the northern Campos Basin (Brazil).
- The framework of rift faults is interpreted, and the relative age of fault nucleation is defined.
- Basement lithotypes, structural style, and age are correlated to the onshore Cabo Frio Tectonic Domain.
- Two basement lithotype domains guide the distribution of rift-related strain.
- Intra-basement structures were extensively exploited through brittle reactivation during rifting.

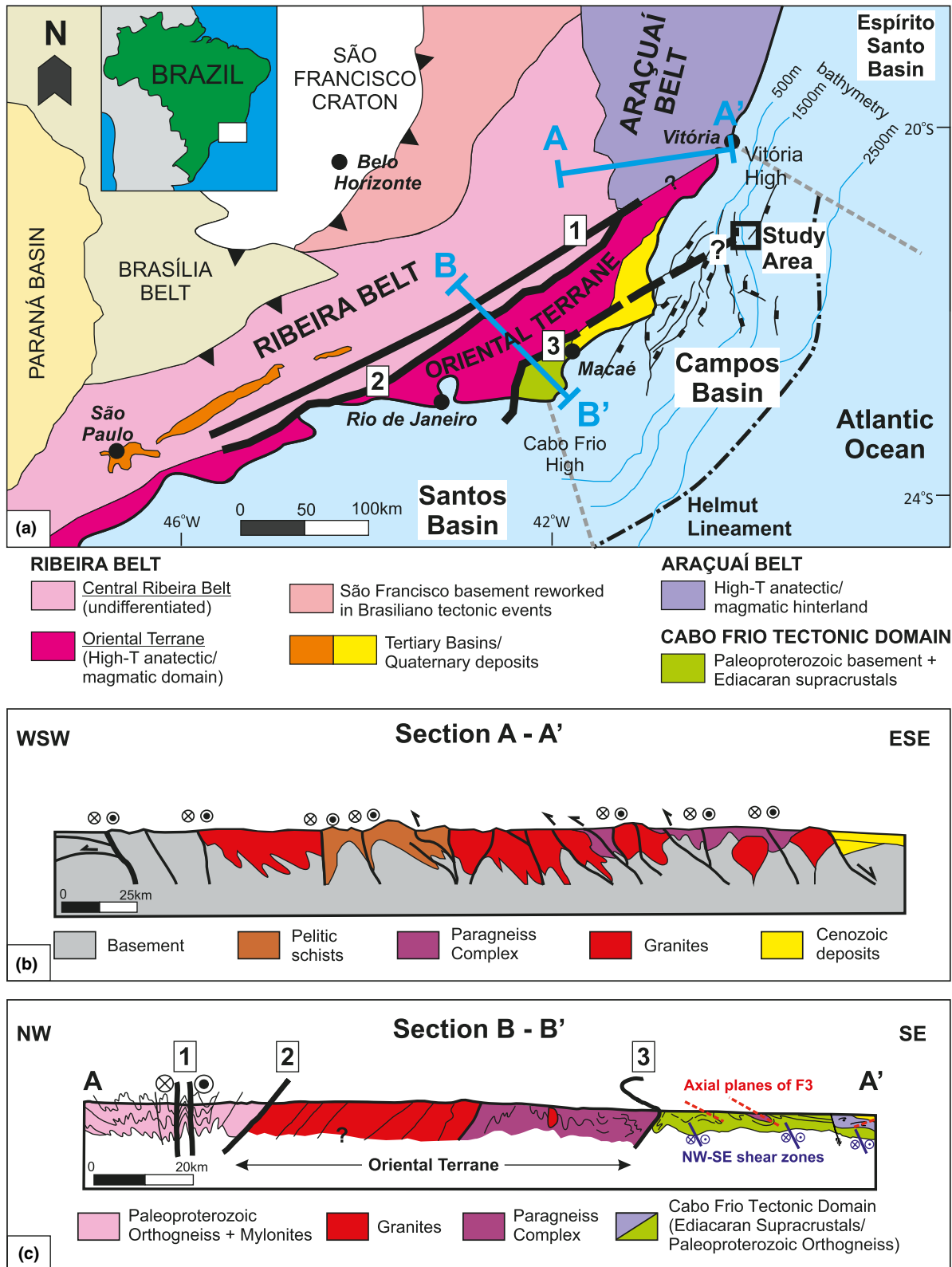
of seismic facies and discrete intra-basement reflections calibrated for lithotype in wellbore data. From this, basement geology and the character of the interactions between extensional tectonics and pre-existing basement heterogeneities are analysed. In addition, novel data regarding basement composition, structure and age were correlated with the known tectonic units of the basement onshore, thus contributing to enhance the scientific debate on pre-breakup reconstructions of the Western Gondwana and the evolution of the Brazilian continental margin.

# 2 | GEOLOGICAL SETTING

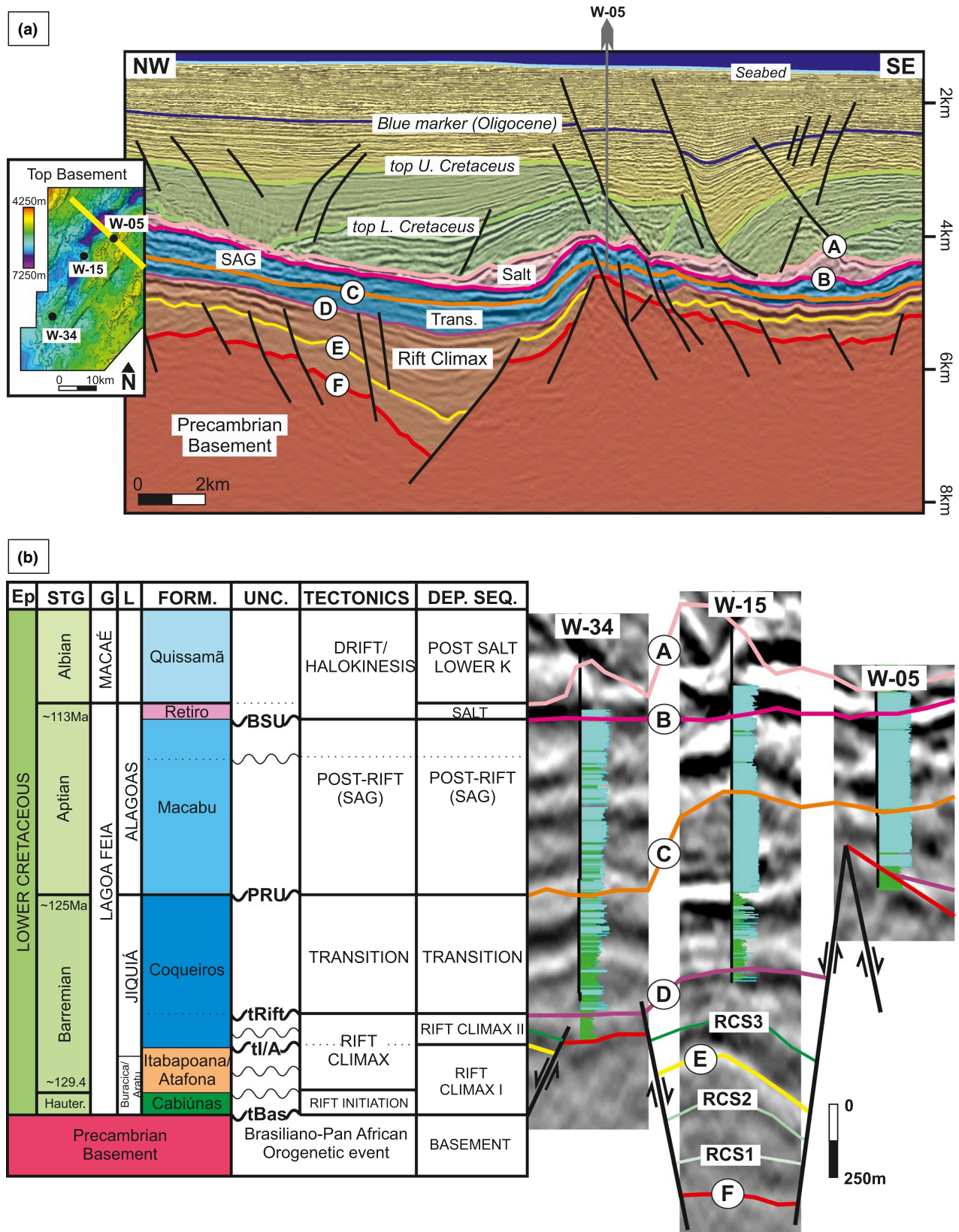
The study area is located in the northern part of the Campos Basin, 70 km offshore East Brazil (Figure 1a). The Campos Basin is part of the Central Segment of the South Atlantic Ocean (Moulin et al., 2010; Torsvik et al., 2009). Its stratigraphy includes Early Cretaceous to recent sediments (Figure 2a). The geometry of the internal structural highs and lows of the basin is controlled by the offshore projection of NE-SW and NNW-SSE basement structures (Fetter, 2009). Onshore, the NE-SW trend corresponds to predominantly Neoproterozoic metamorphic and magmatic rocks of the Mantiqueira Province (Almeida et al., 1981). The NNW-SSE trend consists of networks of brittle structures, whose origin and constitution are not yet established (Calegari et al., 2016).

## 2.1 | Basement

The study area is located in the offshore extension of the Ribeira/Araçuaí Belts and the Cabo Frio Tectonic Domain (Figure 1a; Egydio-Silva et al., 2018; Heilbron et al., 2008;



**FIGURE 1** (a) Onshore and offshore geological setting of the Campos Basin. Offshore geology modified from Fetter (2009) and Silva et al. (2004); Helmut Lineament according to Dehler et al. (2016). Onshore geology modified from Egydio-Silva et al. (2018) and Schmitt et al. (2016). (b) geologic section A–A' represents the southern part of Araçuaí Belt (adapted from Alkmim et al., 2006). (c) geologic section of the northern sector of Ribeira Belt and the Cabo Frio Tectonic Domain (adapted from Heilbron et al., (2008) and Schmitt et al., (2016). NE-SW Structures: (1) Além Paraíba Shear Zone; (2) Central Tectonic Boundary; (3) Cabo Frio Tectonic Limit (CFTL)



**FIGURE 2** (a) NW-SE geologic cross-section of the study area, including the entire sedimentary column of the Campos Basin and main pre- and post-salt structures. Location map shows the position of the cross-section and the wells shown below. (b) stratigraphic and tectonic framework of the Campos Basin in the study area. Lithostratigraphy, ages and tectonics are based on Winter et al. (2007) and Prosser (1993). Wells shows the near-well seismic signature and GR log. Colours coding of the seismic stratigraphic marker horizons and depositional sequences is continued throughout. Mapped seismic horizons: A – tSalt, B – bSalt, C – PRU (Post-Rift Unconformity), D – tRift, E – ti/A (top Itabapoana/Atafona fms.), F – tBas (top basement). Rift Climax Surface (RCS) 1, 2, and 3 are local unconformities within the rift climax sequence. Ep = Epoch, STG = Stage, G = Group, and L = Local stage. GR log scale from zero (blue) to 150 gAPI (green)



Schmitt et al., 2008). According to Brito Neves et al. (1999) and Schmitt et al. (2018), these belts correspond to high-grade metamorphic and magmatic rocks that resulted from a succession of accretionary and collisional episodes, attributed to the Brasiliano-Pan African tectonic events that were a consequence of Neoproterozoic-Cambrian amalgamation of western Gondwana blocks (the São Francisco and Congo/Angola cratons). Although Araçuaí (Figure 1b) and Ribeira (Figure 1c) have differences in tectonic fabric (N-S and NE-SW oriented respectively) and strain regimes, they both evolved during the same tectonic events (ca. 0.65–0.5 Ga), and can be considered as two segments of the same orogenic belt (Stanton et al., 2019 and references therein).

The Oriental Terrane (eastern Ribeira Belt) and the Cabo Frio Tectonic Domain (CFTD) can be extrapolated offshore to the study area, following the trends of their tectonic boundaries (Figure 1a; Egydio-Silva et al., 2018; Schmitt et al., 2016). The former is constituted by low P-high T Neoproterozoic para- and ortho-derived gneisses intruded by several magmatic bodies, with NE-SW fabrics that include foliation, folds and other ductile structures generated during a protracted evolution from ca. 650–500 Ma under a right-lateral transpressional regime (Ebert & Hasui, 1998; Heilbron et al., 2008; Schmitt et al., 2016). Its northwest boundary with the Central Ribeira Belt is defined as a major NE-SW shear zone, the Central Tectonic Boundary (Almeida et al., 1998), parallel to the Além Paraíba Shear Zone (Figure 1a and c; Heilbron et al., 2008).

Towards the coast, the Oriental Terrane is in contact with the contrasting Cabo Frio Tectonic Domain (CFTD). This CFTD mainly comprises Paleoproterozoic orthogneisses (2.0 to 1.94 Ga) tectonically interleaved with medium to high P - high T Neoproterozoic para-derived gneisses, both migmatized (Figure 1c; Schmitt et al., 2004, 2008, 2016). The metamorphism and coeval ductile structures were developed between 550 and 490 Ma as a result of a plate collisional event referred to as the Búzios Orogeny (Schmitt et al., 2004), confirming a tectonic rejuvenation towards the offshore. The CFTD has a NW-SE to N-S structural grain, orthogonal to the adjacent Oriental Terrane (Schmitt et al., 2004, 2016). Their contact is interpreted as a ductile shear zone folded by  $F_3/F_4$  (CFTL in Figure 1a,c). The Neoproterozoic paragneiss preserves  $S_{1+2}$  in isoclinal intrafolial structures, refolded by recumbent  $F_3$  folds with a subhorizontal axial plane spaced cleavage. The Paleoproterozoic orthogneiss develops only localized high strain sub-vertical NW-SE zones (Schmitt et al., 2004, 2016). The contrasting rheology of the basement (Paleoproterozoic orthogneisses) and the supracrustals (Neoproterozoic paragneiss) generates a complex geometry summarized as top to E-SE Km-scale fold nappes in the latter and sub-vertical high strain zones in the former (Figure 1c; Schmitt et al., 2008).

The offshore extension of the CFTD along with its geometric/tectonic connections with the Ribeira Belt and their African equivalents are still unclear since a significant part occurs within the submerged continental margins. Egydio-Silva et al. (2018) and Cavalcante et al. (2019) suggest that the CFTD extends northwards to a position of 21°S on the Brazilian margin where it lies beneath the Campos Basin, and reaches as far as the southern part of the West Congo Belt, sharing similar tectonic-metamorphic evolution as ca. 550–500 Ma (Monié et al., 2012; Schmitt et al., 2016). Offshore drilling in the Cabo Frio High (Figure 1a) recovered calc-alkaline orthogneiss samples, with igneous zircon cores of 1.98 to 1.96 and 0.5 Ga thin metamorphic rims compatible with the Paleoproterozoic orthogneiss of the CFTD (Carmo et al., 2017). These ages are also coincident with the basement of the Angola Block in the actual African continental counterpart (Schmitt et al., 2016).

Evidence of basement-related shear zones being reactivated during South Atlantic rifting is documented in the onshore and offshore portions of Campos Basin (Chang et al., 1992; Dehler et al., 2016; Fetter, 2009; Savastano et al., 2017). Stanton et al. (2010) studied magnetic features across the onshore and offshore and showed that syn-rift faults and dikes are parallel to the NE-SW Ribeira Belt shear zones, but are orthogonal to the CFTD structural grain. Later, Stanton et al. (2019) concluded that the presence of heterogeneous (layered) crust of the CFTD or a more homogeneous crust of the Ribeira/Araçuaí belts determined the temporal and spatial distribution of the deformation, and as a consequence, the necking geometry, subsidence and sedimentary evolution of the margin.

## 2.2 | Campos Basin

The stratigraphic record of the Campos Basin is divided into three tectonostratigraphic mega-sequences: Non Marine Rift, Transitional Post-Rift, and Marine Drift (Cainelli & Mohriak, 1999; Winter et al., 2007). The Pre-Salt sedimentary units here studied belong to the Non-Marine Rift unit and are constituted by four seismic depositional sequences that approximately corresponds to the tectonic stages of the rifting, as defined by Prosser (1993): rift initiation, rift climax, transition and post-rift. These sequences are bounded by regional unconformities named Salt Base Unconformity (SBU), Post-Rift Unconformity (PRU), Top Rift (tRift), Top Basement (tBas), and the Top Itabapoana/Atafona Formations (ti/A) seismic horizon, whose seismic expressions were mapped throughout the studied area (Figure 2b).

The rift initiation stage (Hauterivian) is marked by tholeiitic volcanic activity, represented by the Cabiúnas Formation (Mizusaki et al., 1992). The rift climax stage (Early Barremian) is related to the development of an extensive

system of half-grabens in which a series of interconnected lake basins persisted, becoming periodically isolated during times of reduced lake-level developing local and regional unconformities. Sediments deposited during this stage are proximal siliciclastics to continental mudstones of Itabapoana and Atafona formations (Bertani & Carozzi, 1985a, 1985b; Mizuno et al., 2018; Thompson et al., 2015). They are succeeded by bioclastic rudstones and grainstones of the Coqueiros Formation, which was initially part of the rift transition stage (Mizuno et al., 2018; Winter et al., 2007). Later, Olivito and Souza (2020) assigned the basal carbonate section of the Coqueiros Formation to the rift climax stage (Figure 2b). The rift transition stage (Late Barremian) is represented by the upper section of the Coqueiros Formation that lies directly over the tRift Unconformity (Figure 2) and is limited on the top by the regional Post Rift Unconformity (PRU – sensu Muniz & Bosence, 2015). The Macabu Formation (Aptian) comprises argillaceous and carbonate laminites plus spherulitic carbonate deposits and crusts (Lima & De Ros, 2019; Wright & Barnett, 2015), and represents the post rift (SAG) stage (Figure 2). The Macabu and Coqueiros formations constitute the main hydrocarbon reservoirs of the Pre-Salt sequence, whose petrophysical properties were strongly impacted by structurally controlled hydrothermal alterations (Lima & De Ros, 2019; Lima et al., 2020).

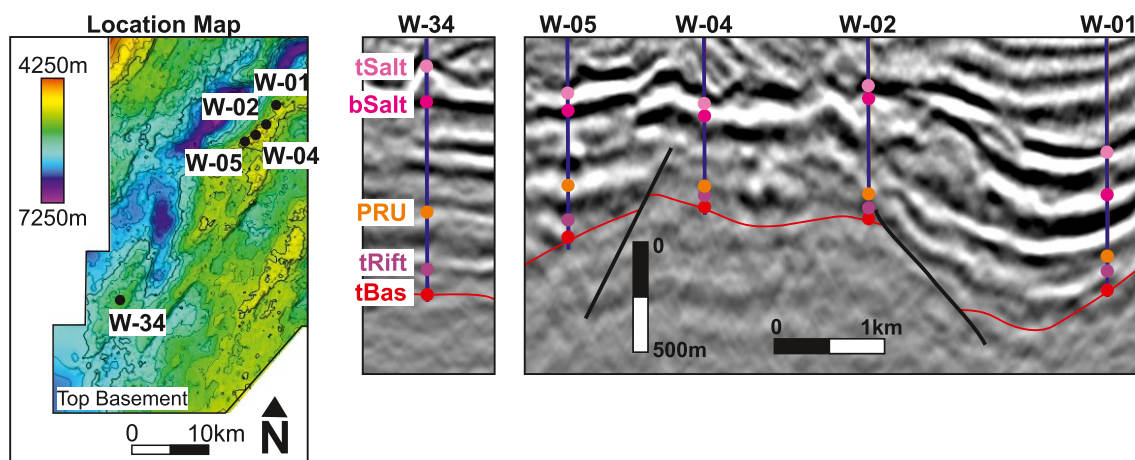
Systematic fault mapping has only been undertaken to date in the shallow water area of the Campos Basin (Figure 1a). The main structural features of the top basement are horsts and grabens delimited by steep normal faults that were active during the Early Cretaceous rifting (Chang et al., 1992). Fault blocks are bounded by alternating eastern and western-dipping NNE normal faults, which are laterally continuous for long distances and have throws of as much as 2,500 m (Guardado et al., 1989). According to Heine et al. (2013), the main extension direction of rifting changes from NW-SE during rift initiation to WNW-ESE during rift climax

(Barremian). The rotation of extension direction was subsequently endorsed by Savastano et al. (2017) in their study of dyke emplacement and brittle reactivation in outcrops of the CFTD basement rocks in the coastline near the southern limit of Campos Basin.

### 3 | DATA AND METHODS

This work is based on 3D seismic interpretation of a commercial 3D streamer Pre-Stack Depth Migration (PSDM) dataset, which images to 10 km depth. The seismic data covers an area of ca. 1,000 km<sup>2</sup> and consists of a merge of two seismic surveys acquired by PGS Geophysical in 2005 and 2010, followed by a depth migration (Kirchhoff TTI) processing sequence. The seismic data are zero-phase processed and the seismic sections are presented with SEG positive standard polarity (downwards increase in acoustic impedance is represented by a positive reflection event (peak) plotted black on a variable density display). Inlines and crosslines of the seismic survey are E-W trending and N-S trending, respectively, spaced at 12.5 m (inlines) and 6.25 m (crosslines). Within the Pre-Salt succession, the 3D seismic has a dominant frequency of 15 Hz and an estimated vertical resolution of 90 m, based on a velocity of 5,400 m/s. Vertical resolution is obtained following the widely accepted definition of resolution limit that corresponds to Rayleigh's criterion of peak-to-trough separation at  $\lambda/4$  (Kallweit & Wood, 1982).

Well logs and geological markers from 36 hydrocarbon exploration and development wells were used to calibrate the seismic horizons within the sedimentary section. Five wells penetrated basement (Figure 3), for which sidewall core samples were described and thin sections extracted. Sidewall core samples from well W-01 were used for geochronological analysis. Zircons were separated from the whole rock by mechanical crushing, milling, heavy-liquid and then



**FIGURE 3** Location and seismic signature of wells that reach the basement top. Well markers refer to the main unconformities and mapped horizons as presented in Figure 2b

magnetic processed. Zircons were collected from less magnetic fractions, then assembled in epoxy-plates and polished to expose the cores, according to procedures suggested by Böhn et al. (2009). These crystals were analysed using an LA-ICP-MS (Laser Ablation Inductively Coupled Plasma Mass Spectrometry) at the University of Rio Grande do Sul (UFRGS). Data regression analysis was done with Isoplot 3.0 (Ludwig, 2003).

Six main seismic horizons within the Pre-Salt layers (PRU, tRift, tI/A and tBas) and the evaporites (tSalt and bSalt) were mapped throughout the 3D seismic survey (Figure 2a). Horizon interpretation was firstly made from well markers between seismic-calibrated wells then expanded across the study area, where the truncation of seismic reflections guided the interpretation of the unconformities. Seismic horizons represent the main unconformities within the Pre-Salt succession plus the lower and upper limits of the salt layer. In addition, three internal unconformities (RCS1, RCS2, and RCS3) related to the rift climax stage were interpreted within the depositional lows (Figure 2b). The interpreted horizons were used to build structural and isopach maps.

The top basement in the seismic data is usually an interface between two seismic units with contrasting amplitude content and coherence levels. The layered character of the overlying sedimentary rocks is distinguished from the usually transparent to anastomosing reflections of the basement rocks. This boundary is normally expressed on the seismic data as an acoustically harder surface (increasing acoustic impedance downward) concerning the overlying sediments (Figure 3).

At least two mapping directions were used for fault interpretation for a better constraint of fault and basement structure. Seismic horizons and the structural network of both intra-basement and rift structures were then used to build a 3D structural model. Faults are represented as triangulated surfaces (250m mesh), from which dip angle and dip direction were calculated in every node, allowing further construction of equal-area lower-hemisphere stereographic diagrams (stereograms).

Rift faults have their relative age of slip obtained firstly from the observation of syn-kinematic wedges (divergent) sedimentary packages in the hanging wall of the faults, systematically thickening towards the main fault (see Prosser, 1993). Secondly, when syn-kinematic wedges are absent, we assumed that fault nucleation occurred near the horizon on which the fault exhibits its maximum throw (Walsh & Watterson, 1988). Seismic reflectors exhibiting a divergent pattern against a fault plane are the most reliable indication of syn-depositional fault slip and thus a time frame of fault activity since we know the relative age of the sediments (Prosser, 1993), although caveats apply when rift basins are sediment starved (Cartwright, 1991).

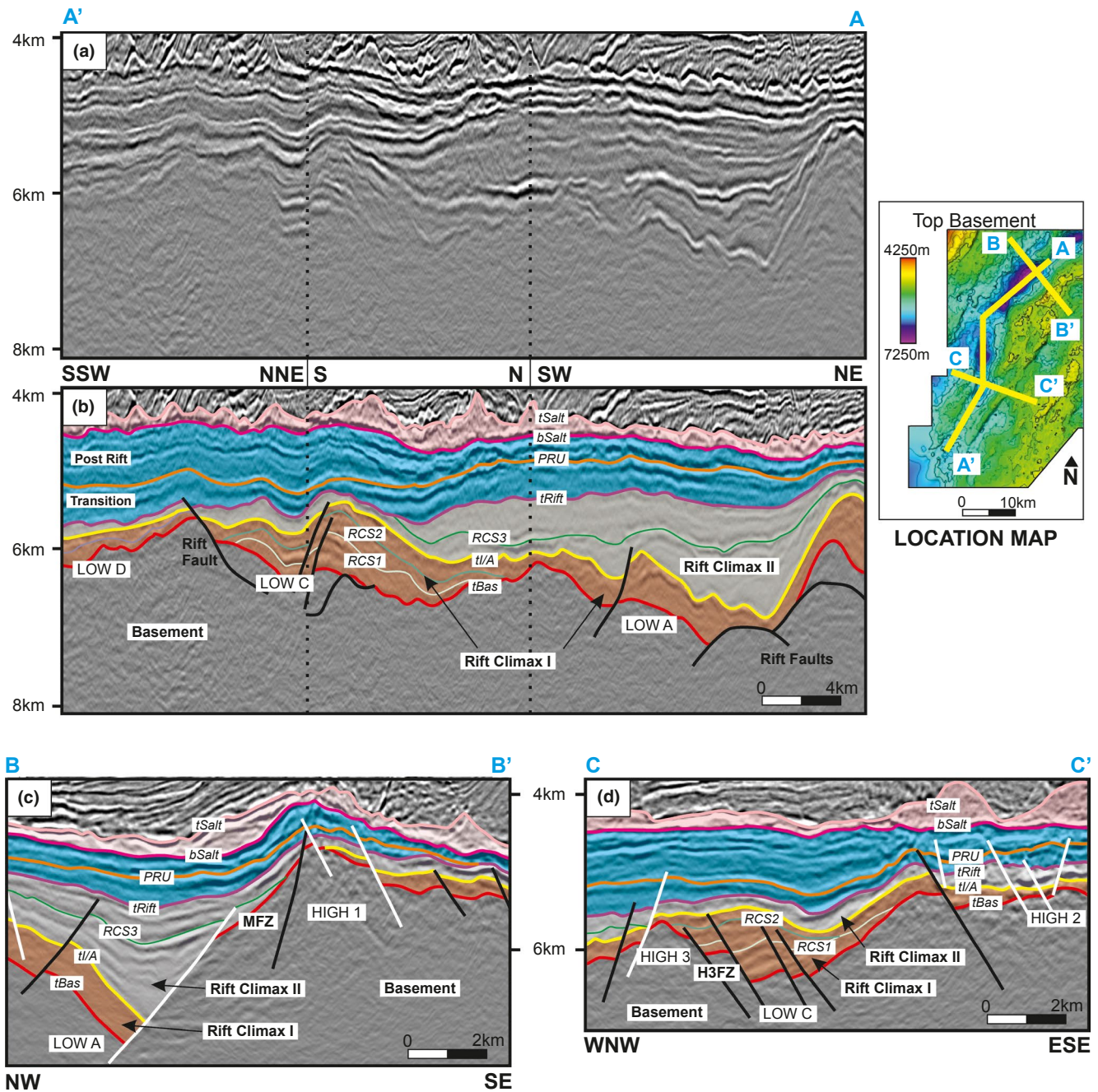
It is worth noting that no pre-rift sediments have been recorded in the Campos Basin (Szatmari & Milani, 2016; Winter et al., 2007) and the deposits attributed to the rift initiation age in our study area consist of erratically distributed and thin (up to 50 m thick in wells) volcanic layers of the Cabiúnas Formation. To constrain the interpretation of fault age with the creation of accommodation space during fault activity, isopach maps of the Rift Climax I and II seismic-depositional sequences were built and superposed on the fault networks. For descriptive purposes, we refer to “fault nucleation” for both mechanisms of reactivation of pre-existing ductile intra-basement structures/metamorphic foliation or the nucleation of rift faults that cross-cut the pre-existing basement anisotropy. For kinematic analysis purposes, we observed fault heaves and the displacement on tBas and tI/A horizons, initially assuming a pure dip-slip movement in the fault segments, with no later reactivations. Unfortunately, more accurate methods of kinematic analysis could not be used in our dataset. For example, expansion index, throw-depth and throw-distance plots (e.g. Cartwright et al., 1998; Reeve et al., 2015) could not be applied since the mapped horizons consist of unconformities.

## 4 | RESULTS

### 4.1 | Seismic stratigraphy

The Pre-Salt sedimentary record was divided in four seismic-depositional sequences that approximately equate with the previously defined lithostratigraphic units and tectonic phases (Figure 2): (a) Rift Climax I (RCI), (b) Rift Climax II (RCII), (c) Transition, and (d) Post-Rift. However, the top of the Cabiúnas Formation (i.e. the top of the rift initiation stage) does not have a correlative seismic horizon. For this reason, the tI/A horizon was employed to subdivide the depositional sequences that are equivalent to the rift initiation and climax stages in Rift Climax I and II sequences. Consequently, the RCI sequence includes the volcanoclastic rocks of the rift initiation (Cabiúnas Formation) and the siliciclastic deposits of the early rift climax stage (Itabapoana/Atafona Formations), whilst RCII contains the carbonatic basal section of the Coqueiros Formation (Figure 2b), in accordance with Olivito and Souza (2020). The distribution of rift climax sediments is strongly controlled by the rift-related structural highs and lows (Figure 4), which in turn are defined by the major fault zones (Figure 5a). The internal unconformities are noticeable within the depositional lows but not in the structural highs. Consequently, wellbore data provides the best evidence for the limit between RCI and RCII (i.e., the tI/A seismic horizon), based on the lithological contrast between





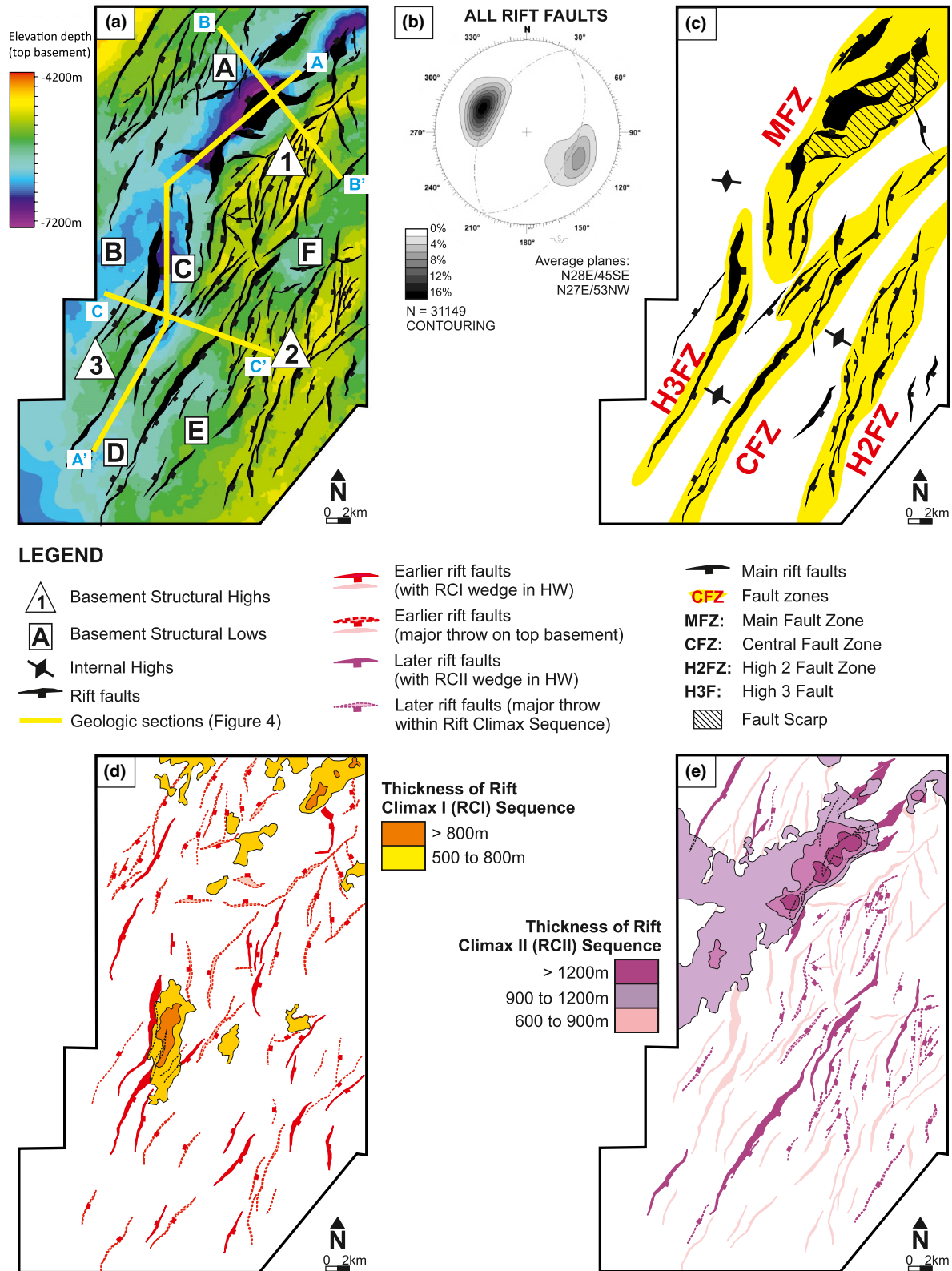
**FIGURE 4** Geologic sections showing thickness variations of rift climax packages and their relationship with rift faults. (a) uninterpreted and (b) interpreted A-A' kinked seismic section across the Lows A, C and D (Figure 5a) presenting the thickness variations of Rift Climax (RC) Strata. Notice the northward depocenter migration from RCI to RCII seismic-depositional sequences. (c) interpreted B-B' dip section across the Low A showing syn-kinematic wedges of RCII against the Main Fault Zone (MFZ). (d) C-C' dip section across the Low C presenting syn-kinematic wedge of RCI sediments against the High 3 Fault Zone (H3FZ). In (c) and (d), fault traces in black represent earlier faults while faults in white correspond to late rift faults (see Figure 5 and text for explanation)

siliciclastics of the RCI and the carbonates of RCII in the structural highs.

The two internal unconformities within the RCI sequence (RCS1 and RCS2 – Figure 2b and d) only occur within the Low C, which is the only depocentre limited by N-S faults (Figure 4b,d). The syn-tectonic character of the RCI is evidenced by the syn-kinematic wedges in the hanging wall of

the H3FZ (Figure 4d). The RCII sequence is bounded by tI/A and tRift horizons. The tI/A horizon marks an abrupt change in the lithology (siliciclastics to carbonates) and in the position of the depocentres, as the available accommodation space migrates northwards along the strike of the Main Fault Zone (MFZ – Figure 5c). Syn-kinematic sedimentation of the RCII is well-illustrated in Figure 4c, where a wedge-shaped





**FIGURE 5** Maps of structural framework, top basement compartmentalization, and relative age of rift-related faults. (a) top basement contour map and rift faults showing the structural compartments with respect to basement highs (letters) and lows (numbers); (b) stereographic projection of rift-related faults; (c) rift fault zones and internal highs; (d) rift faults nucleated during Rift Climax I and (e) Rift Climax II sequence, including the main depocentres of both sequences. Rift faults from (d) are shown dimmed in map (e), so these two fault populations in (e) are the set of rift faults shown on (a). The width of fault segments is the fault heave at the top basement horizon

package is observed in the hanging wall of the MFZ. A third internal unconformity (RCS3) is mapped within the RCII sequence. The sedimentary thickness above and below RCS3 reinforces the observed changes in the accommodation space towards the end of the rift climax stage (Figure 4b).

## 4.2 | Rift faults and structural compartments

Over 100 faults that displaced the top basement horizon (tBas) were mapped within the study area (Figure 5a). The faults display a dominantly NE-SW orientation (average of N28E) and primarily dip to the SE, with a subset ranging from N-S to NE-SW, with a common dip to the west, suggesting that they are a conjugate set to the dominant normal faults (Figure 5b).

Four fault 'zones' are here delineated and named where fault traces are clustered as a linear array of structures that, in most cases, define the limits between less deformed structural highs and lows (Figure 5c). The fault zones comprise those with the highest throws and greatest length. The term fault zone is widely used to describe related fault segments restricted to a relatively narrow zone (Peacock et al., 2000 and references therein, Childs et al., 2009), but here we use this term more generally to encompass a network of related seismically observable faults that form noticeable 'corridors' in map view. The fault zones Main Fault Zone (MFZ), Central Fault Zone (CFZ) and High 3 Fault Zone (H3FZ) demarcate the structural highs and lows and comprise hard-linked structures. In contrast, the High 2 Fault Zone (H2FZ) constitutes the High 2 and show most of its segments as soft linked faults, with smaller throws compared to other fault zones. In terms of internal geometry in map view, the fault zones exhibit an anastomosing pattern, except for CFZ and its mostly collinear segments (Figure 5c).

The majority of mapped faults are interpreted as having their main activity phase during RCI (Hauterivian to Barremian). Estimation of the relative age of faulting is based on syn-kinematic wedges of RCI or having their highest throws between the tBas and the tI/A horizons. Faults of this age are widely distributed within the study area (Figure 5d). Coeval hanging wall depocentres (>500 m thick) to these faults are isolated and occur in the downthrown blocks of N-S and NE-SW fault segments of, respectively, H3FZ and MFZ. However, the most significant syn-kinematic wedges are observed in the hanging wall of the H3FZ, and comprise nearly 1,000 m of RCI sediments (Figure 4d). The remaining mapped faults are dated as having their main activity phase during RCII (Barremian), based on the same criteria used for RCI faults. These faults mostly occur within the eastern half of the mapped area. Related depocentres comprise up to 1,400 m thick sedimentary intervals that are contiguous along the hanging wall of the MFZ and extend

further to the SW and W (Figure 5e). Well-developed syn-kinematic wedges of RCII occur against the MFZ (Figure 4c). Importantly, although there is no difference in the average strike direction between faults of RCI and RCII, this is not true for faults with syn-kinematic wedges, of which RCI faults strike NNE-SSW and RCII faults strike at NE-SW (Figure 5d,e).

Structural High 1 is the most prominent, characterised by a horst complex with synthetic and antithetic secondary faults that gently slope eastward (Figure 5a). It is separated westwards from the Low A by a NW-dipping master fault named Main Fault Zone (MFZ). The MFZ consists of a segmented, hard-linked fault array (Figures 4c and 5c), with frequent dip-linkage in profile, with up to 2000 m cumulative displacement and a relatively low dip angle (mean of 30°). In contrast, the southern tip of the MFZ shows N-S soft linked faults with steeper planes (65° avg.), which defines the boundary with the Low C along with the H3FZ. The eastwards limit of Structural High 1 is defined by the Central Fault Zone (CFZ).

Structural High 2 is an NNE-SSW elongated horst bounded by non-collinear faults that is evident in a staircase geometry of the tBas horizon in profile view. Structural High 3 is a small basement feature in the SW part of the mapped area (Figure 5a). It is limited eastwards by a pair of low angle (30°) normal faults in which strike direction changes from NNE to N-S towards the North, and westwards by a ramp with minor antithetic faults that merges with the H3FZ (Figures 4d and 5c).

The structural lows are characterized by half-graben geometries with dominantly NNE-SSW striking axes, except for Low C which strikes N-S (Figure 5a). Low A is the most pronounced depression at the level of the tBas horizon. Interestingly, it is the only low for which the faulted border is to the East, given by the MFZ master fault. The westwards ramp of Low A displays antithetic faults to the MFZ striking NE-SW and NNE-SSW. Fault slip in the MFZ and the coeval creation of accommodation space extend up to the base of the post-rift strata (Figure 4b,c). Low B is only partially represented in the study area and its faulted limit to the west is interpreted to be similar as on the lows C, D, E and F. Their faulted limits are given by the H3FZ for lows C and D, and by the CFZ for lows E and F (Figure 5a).

## 4.3 | Interpretation of intra-basement seismic facies and structures


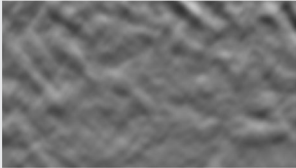
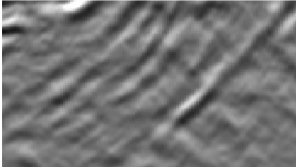
We mapped and classified the intra-basement seismic response into three distinctive 'seismic basement' facies by adapting the classical seismic facies interpretation methods outlined in workflows for seismic stratigraphic interpretation (Mitchum et al., 1977) (Table 1). The aim is to represent contrasting degrees of amplitude content and organization of internal reflections. We also identified and mapped planar and volumetric features that might represent geologically

meaningfully boundaries and internal heterogeneities and hence quantify how they are spatially organized.

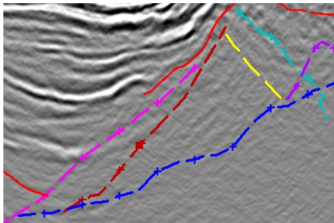
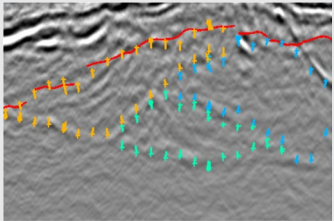
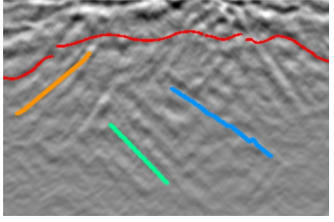
Previous studies have classified basement reflections below rift basins based on (a) binary contrasting reflectivity based on amplitude signatures (Phillips et al., 2016; Reeve et al., 2014), (b) seismic facies (Fazlikhani et al., 2017; Lenhart et al., 2019) and packages (Bird et al., 2014) correlated to main basement units supported by onshore geology,

and (c) types of basement structures based on their 2D geometry (Collanega et al., 2019; Osagiede et al., 2020). Except for Collanega et al. (2019), these studies are all of the North Sea Rift. The classification scheme adopted herein (Tables 1 and 2) aims to combine these already existing methodologies. This approach was required due to lack of direct connection between onshore and offshore geology in the Campos Basin (Figure 1a), in contrast with the slightly less unpredictable

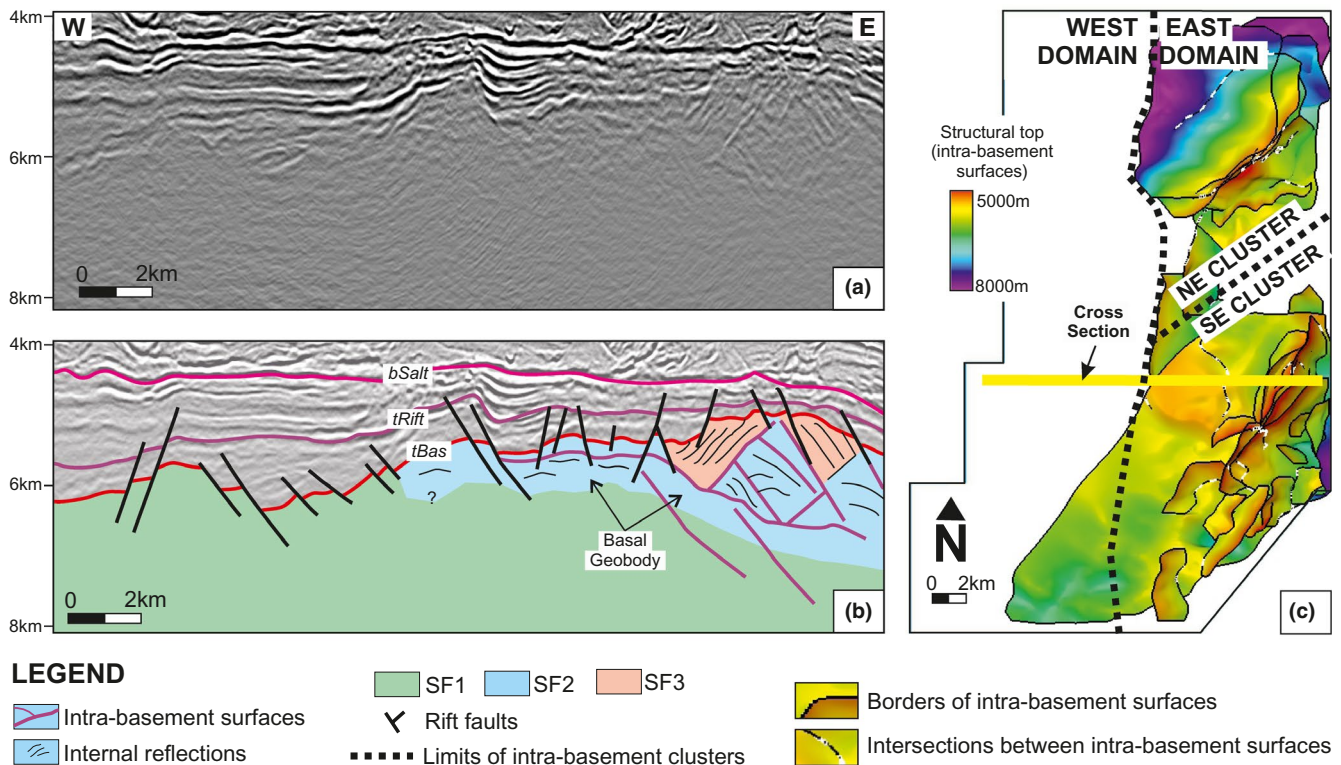
**TABLE 1** Amplitude signature of the seismic facies for basement seismic response.

Facies	Name	Seismic signature	Description
SF1	Homogeneous		Low amplitude (transparent), moderate to high frequency, chaotic to anastomosed reflections
SF2	Moderately heterogeneous		Moderate to high amplitude, low to moderate frequency, anastomosed to sub-parallel reflections, with some internal coherency
SF3	HIGHLY heterogeneous		High to moderate amplitude and frequency, parallel to sub-parallel reflections, highly anisotropic

**TABLE 2** Description of intra-basement features. The continuous red line is the Top Basement horizon.

Feature	Mapped as	Seismic expression	Description	Interpretation
Surface	Fault		Interfaces of contrasting internal reflections (angle, dip direction). Usually, but not always, coincides with geobody's boundary	Narrow to broad ductile shear zones
Geobody	Multi-Z interp.		Geobodies with contrasting internal dip angles/direction that can be mapped in more than one direction	Tectonic lenses with remnant self-organized heterogeneities bounded by shear zones
Internal reflection	Horizon		Consistent and trackable internal reflections, usually enclosed by geobodies	Internal heterogeneities (tectonic foliation?)





**FIGURE 6** The interpretation workflow for intra-basement seismic structure. On (a) uninterpreted and on (b) interpreted seismic section, showing seismic facies (Table 1) and intra-basement features (Table 2). On (c) the 3D network of intra-basement surfaces is tentatively shown in a map view

offshore basement geology based on onshore of the North Sea Rift.

Seismic Facies 1 (SF1) represents the least heterogeneous of the facies, SF2 is moderately heterogeneous, and SF3 represents the most heterogeneous basement with respect to seismic reflectivity (Table 1). These seismic facies are limited by or contain correlatable surfaces, here called Basement Features (Table 2). Specific criteria were established to interpret the basement features, for which a single surface must appear consistently within a range of at least 100 lines and/or traces. The mapped intra-basement surfaces were categorized in three main features (Table 2): (a) planar discontinuities (Surfaces), (b) 3D volumes that are bounded by surfaces (Geobodies), and (c) planes within Geobodies (Internal Reflection). These internal reflections within the geobodies potentially represent internal heterogeneities but that are not necessarily conformable with the external boundaries.

The workflow adopted is described using a seismic section as an example (Figure 6). In a blank section (Figure 6a), we interpreted the tBas horizon and the intra-basement surfaces and geobodies (Figure 6b). Such 2D interpretation is then extended and validated in the 3D space. For every surface-bounded geobody of basement structures, we attribute a seismic facies following Table 1. The network of interpreted surfaces that resulted from the interpretation of intra-basement surfaces is tentatively shown in a map view

on Figure 6c. Notice the absence of structures in the western half of the studied area, in contrast with the highly structured basement in the east. Between these East and West Domains, a roughly N-S boundary is drawn on Figure 6c. Such binary division is also backed in the lithologies described in the rock samples (see Item 4.4).

The self-arrangement of intra-basement surfaces on the East Domain allowed them to be grouped into two distinctive areas, here named Clusters NE and SE (Figure 6c). When dividing the intra-basement structures into two clusters, we considered the quantity and the distinct main strike direction of the intra-basement features, and the contrasting modes of interactions between basement heterogeneities and rift faults. Also, the lack of a clear physical connection across a NE-SW imaginary line that divides the clusters suggests the presence of a geological boundary (Figure 6c). Among the similarities, the NE and SE Cluster of intra-basement structures consist of a low angle ( $<20^\circ$ ) basal geobody over which discontinuities of higher angle are juxtaposed (up to  $45^\circ$ ).

Seismic facies 1 (SF1) is characterized by a chaotic network of low amplitude, moderate to high-frequency seismic response. It dominates the basement seismic response in the West Domain (Figure 6b,c) and in depths higher than 7 km in the East Domain (Figure 6b). Although the SF1 can be simply interpreted as a consequence of the attenuation of the seismic signal below a certain depth, it can be observed both below

the tBas horizon and the heterogeneous SF2 and SF3 seismic facies. SF1 is interpreted as being indicative of a basement that is more isotropic (granitoids or ortho-derived gneiss), which is supported by rock samples (see Section 4.4).

Seismic Facies 2 (SF2) and Seismic Facies 3 (SF3), along with intra-basement surfaces, largely occur in the East Domain (Figure 6). SF2 consists of moderately organized, anastomosing to sub-parallel reflections. Its higher amplitude character distinguishes SF2 from SF1. SF3 has been identified only within geobodies bound by intra-basement surfaces and the tBas horizon. It is characterized by high amplitude, highly anisotropic parallel reflections. Although showing contrasting seismic anisotropies, SF2 and SF3 are interpreted as being comprised of heterogeneous, layered basement rocks units such as foliated metamorphic rocks (e.g. schists and gneisses). The samples obtained in the drilled wells (Figure 3) provided the control that these highly reflective seismic domains are metamorphic and not sedimentary formations.

The three intra-basement features defined in Table 2 represent both internal fabrics and major structural boundaries within the basement rocks units. We interpreted surfaces as ductile shear zones that delimit less deformed geobodies. Below heterogeneous SF2/SF3 a low to very-low dip angle ( $<25^\circ$ ) tabular basal geobody of SF2 is often observed in both NE and SE clusters (Figure 6b). This Basal Geobody is often bounded by surfaces that are conformable with the internal reflections.

#### 4.3.1 | The NE cluster

This group of intra-basement heterogeneities lies under Structural High 1 and in the northern part of Low A (Figure 7), including a master fault represented by the Main Fault Zone (MFZ). The intra-basement surfaces mapped within this cluster have a mean attitude of N43E/21NW and secondarily N49E/30NE (Figure 7f), although their low angle character implies in a highly scattered dip angle pattern. For this reason, a stereogram excluding the surfaces that define the Basal Geobody unit is also shown (Figure 7g).

The overall geometry of NE Cluster can be described as a low angle, NW dipping Basal Geobody, enclosed by an asymmetric antiformal structure (Figure 7d). The base and the eastern flank of the antiform are made of SF2, while the steeper western limb is marked by SF3. The Basal Geobody becomes increasingly shallower towards the East, eventually merging with the eastern flank of the antiform and thus reaching the Top Basement horizon (Figure 7e). The interpretation of these structures suggests that the Basal Geobody has functioned as a ductile detachment for the antiform structure above (Figure 7d,e). This geometry may represent a

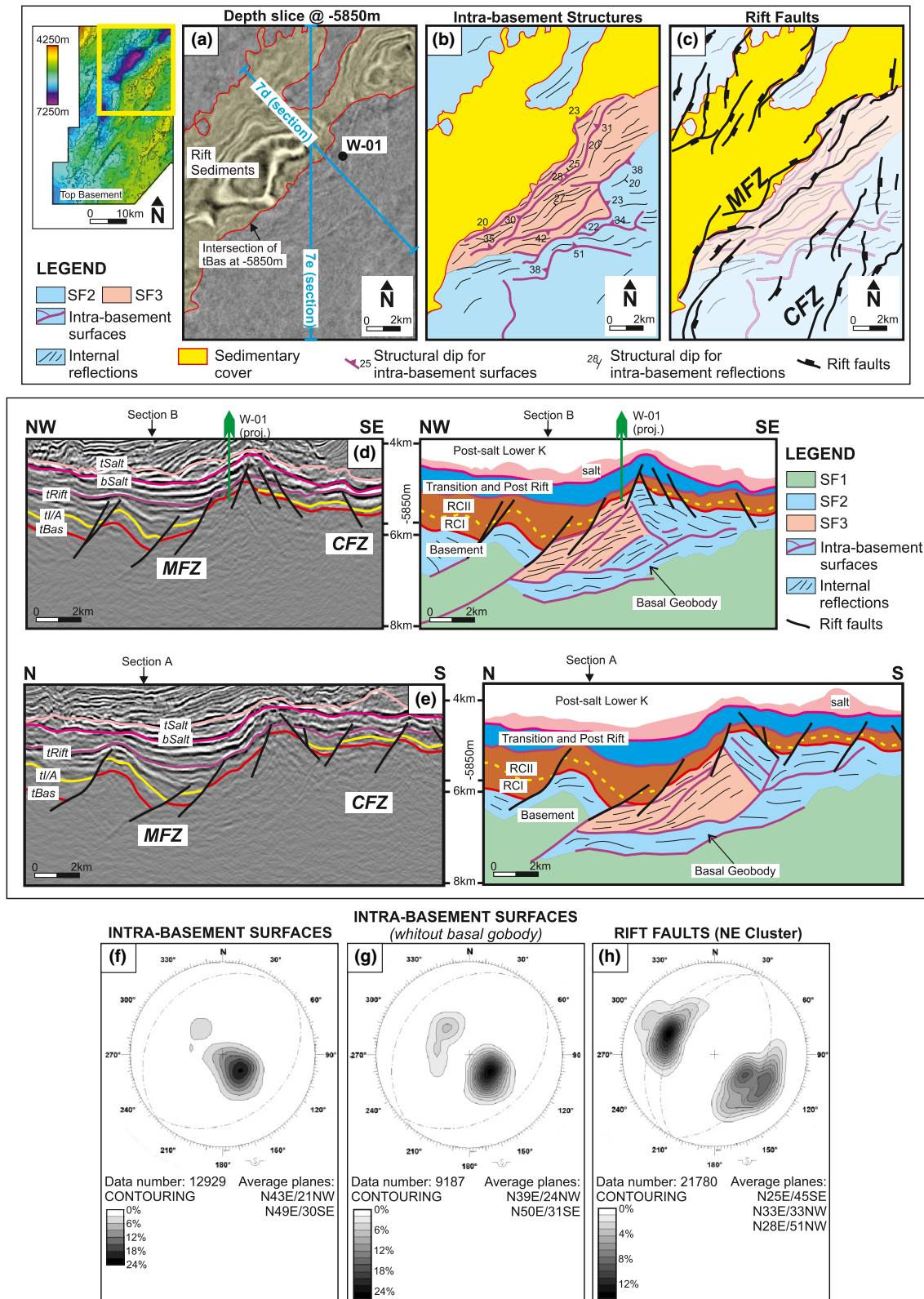
fault-bend fold or a detachment fold with respect to the Basal Geobody with a suggested vergence to NW.

#### 4.3.2 | Integrating rift and basement structures in the NE cluster

The rift faults that overlie the NE Cluster have a main trend of N28E dipping to both NW and SE, sub-parallel (circa  $15^\circ$ ) in strike with respect to the basement structures (Figure 7c,g,h). The rift faults show scattered strike and dips, ranging from N-S to E-W and  $25^\circ$  to  $70^\circ$ , respectively (Figure 7h). Fault segments dipping to the NW represent MFZ segments while faults dipping to the SE are secondary structures on the footwall and hanging wall blocks of the MFZ.

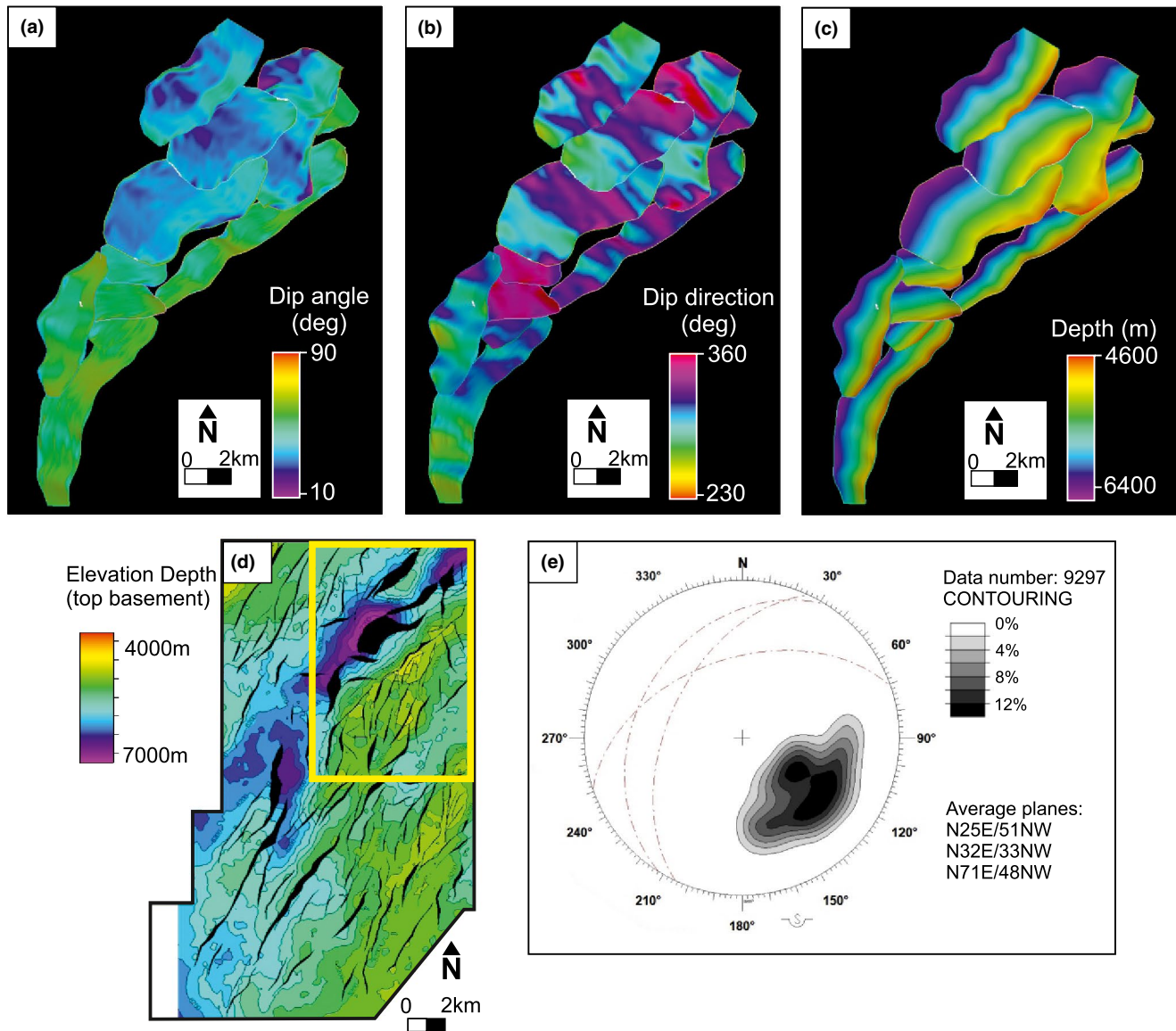
The interplay between reactivation of basement structures and the MFZ is evidenced by the sub-parallelism between fault segments and the basement fabric (Figure 7c-e), and the coeval deposition of syn-kinematic wedges of RCII sediments on the hanging wall of the MFZ (Figure 4c). Fault segments on the southern tip of the MFZ and in the northern tip of the H3FZ are N15E oriented (Figure 8b) and thus define the limits of the Low C, on which the thicker strata of RCI Sequence are deposited (Figures 4d and 5d), implying that these fault segments are probably the oldest in the studied area. Syn-kinematic wedges of RCI sediments occur against the H3FZ (Figure 4d) while the same geometry is observed in sediments of RCII age in the hanging wall of the MFZ (Figure 4c). Consequently, fault segments of MFZ are younger northwards, as suggested by the diachronous thickness distribution of rift climax sediments along the H3FZ and the MFZ (Figures 4b and 5d,e). During the northward propagation of the MFZ, the newly formed segments became progressively oriented from N30E to N60E (Figure 8b), following the basement fabric (Figure 7d,e). Moreover, dip angles decrease northwards, from  $60^\circ$  on southern segments to less than  $30^\circ$  on the northern segments (Figure 8a). Apparently, the ultimately lower angle of basement fabric leads to fault segmentation in the hanging wall of the northernmost segments of the MFZ and inhibited the deposition of thicker sediments of RCII when compared to the central segments of the MFZ (compare Figures 4c and 7e). Also, the obliquity between intra-basement structures and the MFZ segments slightly increases towards the top (compare Figure 8b,c).

On the eastern sector of the NE cluster, rift faults occur as small antithetic (to MFZ) faults dipping SE over the ramp that constitutes the footwall block of the MFZ (Section 7d). In this area, intra-basement structures and the metamorphic foliation occur at an acute angle with respect to the tBas surface, leading to localized reactivation of basement structures during the rifting (Figure 7e). Nonetheless, when moving eastwards along the footwall ramp (see SE sector of Figure 7d),



**FIGURE 7** Depth Slice, geological sections and stereograms for intra-basement structures and rift faults of the NE Cluster. Depth slice at -5850 m shows (a) the seismic amplitude signal, the boundaries of sedimentary cover and the location of geologic sections, (b) dip directions and angles extracted from 3D surfaces representing the intra-basement structures and internal reflections, and (c) basement structures overlapped by the intersections of -5850 m-surface with rift faults. Sections (d - dip) and (e - strike) displays the framework of basement seismic facies and structures. Well W-01, used for petrographic and geochronological analysis, is also shown. MFZ and CFZ are two of rift related fault zones. On the bottom, stereograms of all intra-basement surfaces (f), intra-basement surfaces except basal geobody (g), and rift faults over the NE Cluster (h) are shown





**FIGURE 8** Geometric analysis of fault segments within the Main Fault Zone (MFZ). (a) to (c) show top views of fault segments within the yellow window shown on (d), presenting, respectively, dip angle, dip direction and depth of fault segments. (e) presents the stereographic projection of MFZ fault segments and the main clusters of data. Notice from (a) and (b) the shift on both dip and dip direction northwards along strike

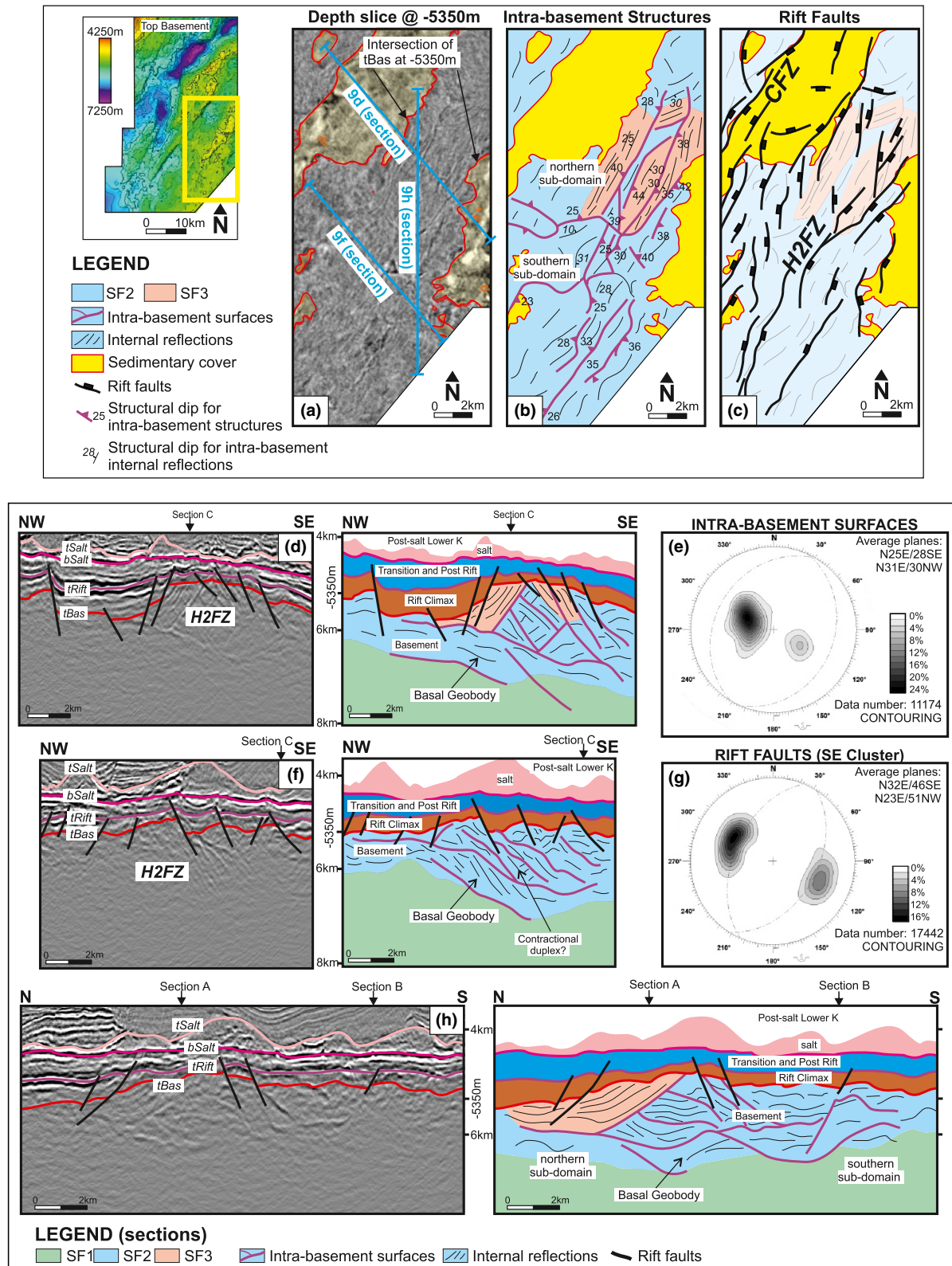
the heterogeneous basement becomes progressively thinner above the homogeneous SF1 and oriented with a high angle to rift faults. Consequently, rift fault tends to nucleate in a geometrical configuration that cross-cuts the metamorphic foliation rather than one paralleling the foliation *i.e.* in an exploitative geometry.

#### 4.3.3 | The SE cluster

This group of basement structures underlies Structural High 2, Low F, and the High 2 Fault Zone (H2FZ). It is delimited on the west by the Central Fault Zone (Figure 9). The

SE Cluster consists of 24 mapped intra-basement surfaces (Figure 6c). It shows similarities with the NE Cluster in the form of a pair of laterally extensive, low angle surfaces (Basal Geobody) over which most of the remaining structures overlie, including an antiformal structure on the northern sector of SE cluster (Figure 9d).

The geometric attributes of structures within the SE Cluster are presented as a stereographic projection on Figure 9e,g, exhibiting a N22E main trend. However, in the central region, a group of WNW-ESE (N dipping) basement structures is observed, dividing the SE Cluster into two areas of contrasting structural styles, referred here as the northern and southern sub-domains (Figure 9b). The northern sub-domain shows a



**FIGURE 9** Depth slice at -5350 m and geologic cross sections showing the intra-basement structures of the SE Cluster. In (a) is presented the seismic amplitude signal, the boundaries of sedimentary cover and the location of geologic sections. (b) shows dip directions and angles extracted from 3D surfaces representing the intra-basement structures and internal reflections. (c) shows intersection planes of rift faults on -5350 m depth slice over the interpretation of basement structures. Below, three geological sections (d, f, and h), shows on left the uninterpreted seismic section with rift-phase faults and horizons, and on right a geological interpretation of basement structures and sedimentary filling. Stereogram (e) presents the intra-basement surfaces, except the Basal Geobody. Stereogram (g) presents the rift faults over the SE cluster

predominance of highly anisotropic basement seismic facies (SF2/SF3) when compared to the southern domain, where SF2 is largely predominant. Apart from the clear contrasts in the structural style observed in the dip sections, the geological section of Figure 9h shows no boundary but a gradual transition from the northern to the southern sub-domains.

The basement structural grain in the SE Cluster is predominantly low angle with boundaries of lenticular shape defined by intra-basement surfaces (Figure 9h) that are generally SE dipping (Figure 9d,f). The Basal Geobody is observed in both sub-domains, similarly to what is observed on the NE Cluster except for the dip direction to SE (compare Figures 7d and 9d). The Basal Geobody is shallower westwards and southwards, where it constitutes basement heterogeneities that have a notably low dip angle (Figure 9d,f).

Basement surfaces of the northern sub-domain often exhibit higher dip angles than the southern sub-domain, and the surfaces dip both to the SE and NW, expressed as an overall slightly asymmetric antiformal geometry (Figure 9d). This interpreted fold has a NNE-SSW axial plane dipping SE, indicating a possible NW-vergence, similar to the antiform in the NE Cluster. In contrast, the southern sub-domain shows exclusively SE dipping basement surfaces, which are less continuous in extent when compared to northern sub-domain. The overlapping geometry of these surfaces which lies with an acute angle over the Basal Geobody is suggestive of a contractional duplex that detaches over the base (Figure 9f).

#### 4.3.4 | Integrating rift and basement structures in the SE cluster

The collection of faults over the SE Cluster consist of a pair of N26E fault populations, mostly dipping to SE ( $46^\circ$ ) and secondarily to NW ( $51^\circ$ ), where the intersection line gently plunges towards the SW (Figure 9g). Most of the rift faults belong to the High 2 Fault Zone (H2FZ), which is distinctive from the remaining fault zones since its fault planes and displacements are generally shorter and smaller, respectively. Thus, their fault segments dip to both directions, defining the main geometry of the High 2, in contrast with the single dip direction observed in the other fault zones (Figure 5c).

The average strike direction of rift faults on SE Cluster is the same as that exhibited by the intra-basement structures (Figure 9e), in contrast with the sub-parallelism observed on the NE Cluster. The parallelism between the rift faults and the shallowest sectors of basement surfaces is prominent in map view and can be also observed in both dip and strike cross-sections of Figure 9.

The observations above are valid for the sectors of SE Cluster where the basement heterogeneities occur up to a certain depth, typically 2 km and at least 1 km below the tBas surface. The

cross-sections of Figure 9 shows that SF2, SF3 and basement features are typically identified to depths up to 2 km below tBas, except in portions of the western sides of Figure 9d,f, where the Basal Geobody occurs directly below the tBas. In these areas, the basement structural grain shows a low to very low dip angle ( $<15^\circ$ ) and was crosscut by rift-related faults.

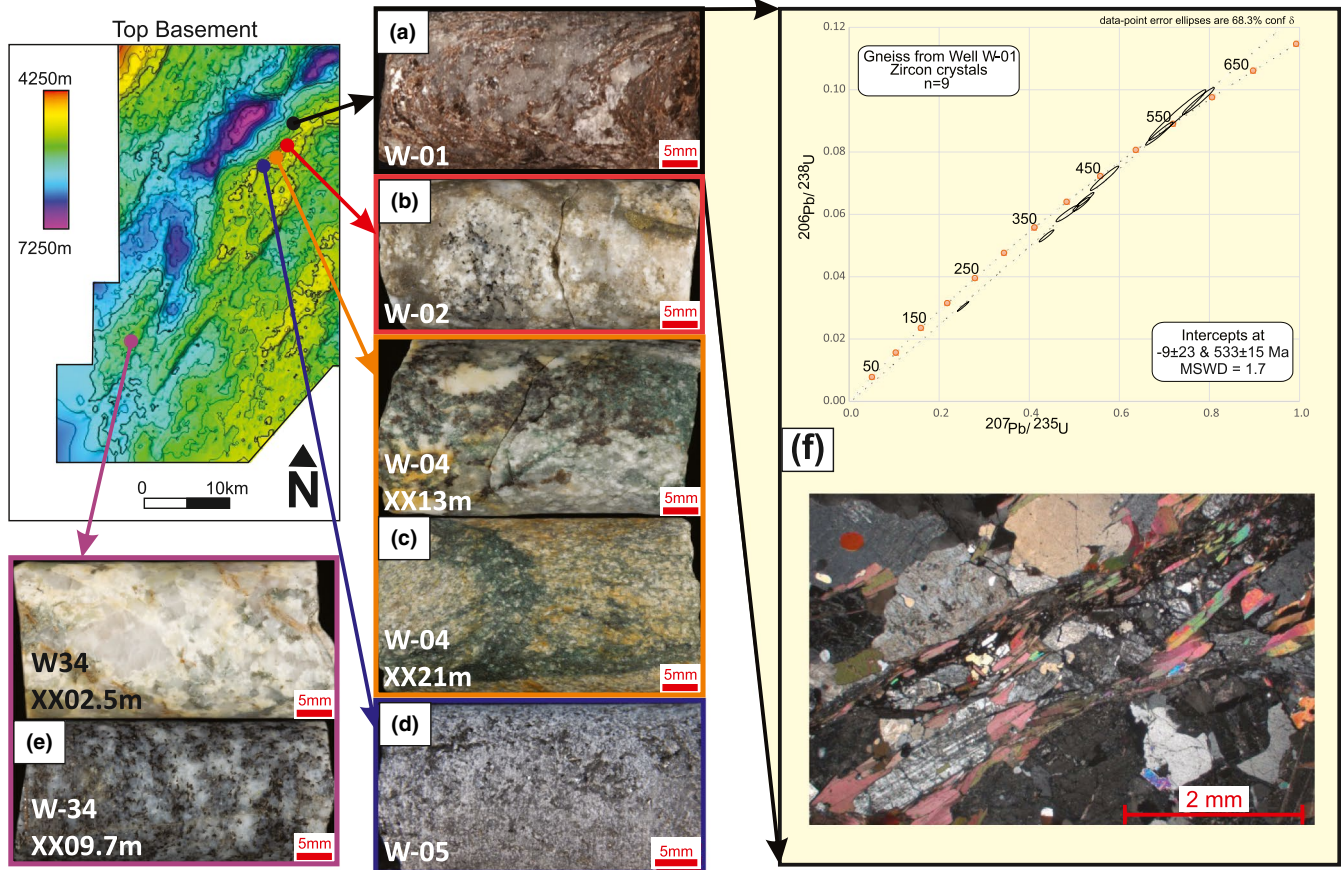
#### 4.4 | Basement samples and geochronological analysis

Five wells recovered basement samples (Figures 3 and 10). Biotite gneiss is the predominant lithology, and all samples show a tectonic foliation marked mostly by phyllosilicates. Veins of coarse-grained quartz and feldspar intergrowth surrounded by mafic rich flakes suggest in situ partial melting and generation of leucosome (veins), therefore migmatitic domains (Figure 10c,d,e). This feature also indicates a subhorizontal compositional banding, related to both the protolith and the subsequent metamorphic event, observed in a single well through 50 m of drilling (Figure 10c). Gneiss samples more enriched in biotite, some with garnet, might be derived from sedimentary protoliths, representing paragneisses. Other gneiss samples show a granitic homogeneous composition that might represent igneous protoliths but could be also leucosome (Figure 10d,e).

In general, samples from wells W-01, 02, 04 and 05 (Figure 10a-d) represent a much heterogeneous set of lithologies in contrast with samples from the westernmost W-34 well (Figure 10e). The latter is also more isotropic and might correspond to homogeneous granitoids, without anisotropy related to gneiss banding and foliation marked by phyllosilicates. This contrast in lithologies and structures is coherent with the basement seismic features in the East and West domains, described previously (Figure 6c).

A sidewall core sample from the basement on W01 (Figure 10a) provided enough material to produce thin sections and to extract zircon crystals for U-Pb geochronology studies (Figure 10f). This biotite gneiss, with a general granitic composition, is mainly constituted by oligoclase and quartz, and secondarily by muscovite, biotite, microcline and zircon. The abundance of phyllosilicates might suggest that this gneiss could have either a sedimentary or an igneous protolith. The granolepidoblastic texture in thin sections implies that this is a medium to a high-grade metamorphic unit with a tectonic foliation (Figure 10f). The projection of the well to the seismic section on Figure 7d indicates that this sample would correspond to the western limb of an antiformal structure, Seismic Facies 3 (SF3), within the NE Cluster. Nine spots were plotted in the Concordia providing an upper intercept of  $533 \pm 15$  Ma, not forced to zero with a Mean Squared Weighted Deviation (MSWD) of 1.7 (Figure 10f). The interpretation of this age is complex because there are no original





**FIGURE 10** Images from basement rocks recovered of five wells in studied area. (a) biotite gneiss, used for geochronological analysis. (b) a leucocratic granitic biotite gneiss from W-02. (c) two images from well W-04 shows a probable migmatitic texture with leucosome and restite rich in biotite and garnet. (d) well W-05 shows a more homogeneous biotite gneiss. The southern/westernmost drill W-34 (e) reached a biotite coarse grained granitoid/gneiss with a discrete foliation and granitic composition. (f) shows the dated sample on top and thin section on bottom shows biotite gneiss with well-preserved granolepidoblastic texture from the northernmost well (W-01)

cathodoluminescence images of the zircons. Although it is most probable that this is a metamorphic age, considering the onshore data from the basement tectonic domains.

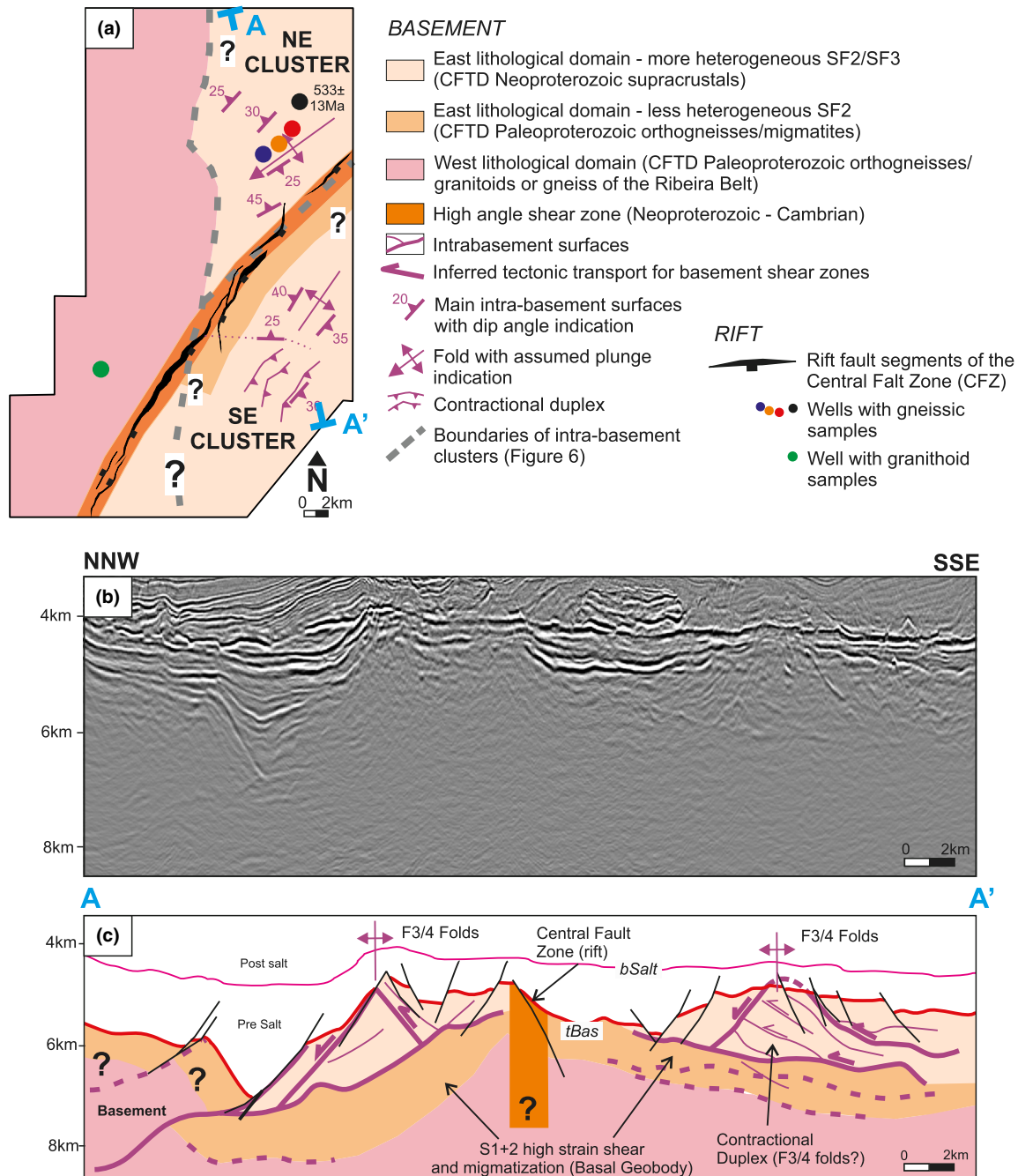
## 5 | DISCUSSION

### 5.1 | Basement geology

The basement occurring immediately below the tBas horizon is divided into two lithological and structural domains: homogeneous (West) and heterogeneous (East) (Figure 11a). However, when observing the basement units in cross-section (Figure 11c), it is noticeable that the homogeneous SF1 that constitutes the West Domain extends under an up to 4 km thick pile of heterogeneous SF2/SF3 basement rocks of the East Domain. This heterogeneous package shows an internal organization consisted of upper SF2/SF3 highly heterogeneous basement over a tabular Basal Geobody of SF2 facies (Figure 11c). Therefore, heterogeneous basement in the East Domain is divided into two sub

domains in depth, more and less heterogeneous, where the more heterogeneous domain is characterized by a complex network of folds and shear zones and the less heterogeneous is constituted by the tabular Basal Geobody (Figure 11c).

Our interpretation is that SF1 on the West Domain represents a more homogeneous set of basement rocks (Figure 11a), characterized by granitoids, equivalent to the drill core from W-34 obtained in this sector (Figure 10e). Based on the observation of the regional geological map and the offshore projection of the CFTL (Figure 1a), two interpretations are possible for the West Domain. In the first, these rocks may represent portions of the Oriental Terrane (Ribeira Belt), which is characterized by the abundance of syntectonic magmatic suites (Egydio-Silva et al., 2018; Heilbron et al., 2008; Schmitt et al., 2016). Alternatively, the West Domain may correspond to the low strain domains of the Paleoproterozoic orthogneisses that constitute the basement in the context of the Cabo Frio Tectonic Domain (CFTD). It is still not clear if the rocks from the West Domain, that extend beneath the East Domain, represent the same basement



**FIGURE 11** Basement geology and tectonic subdivision based on wellbore data and seismic interpretation of intra-basement facies and features. (a) map showing the synthesized basement geology, including structures and the East and West lithological domains at the level of the tBas horizon. (b) uninterpreted A-A' seismic section, from which a (c) A-A' geologic cross-section with the interpretation of the lithologic and tectonic subdivisions of the basement is shown

unit. For this reason, we kept both interpretations for West Domain basement (CFTD Paleoproterozoic orthogneiss or the Oriental Terrane of the Ribeira Belt) in Figure 11.

This contrast between a highly heterogeneous basement in the eastern part of the study area and a more homogeneous unit to the west is taken to suggest a roughly N-S contact between two distinct geological domains (Figure 11a). Our interpretation is that the highly reflective SF2/SF3 facies could

represent the CFTD Neoproterozoic paragneiss and the SF2 facies of the Basal Geobody is equivalent to the migmatites that occur in tectonic contacts between these supracrustals and the underlying Paleoproterozoic basement (Figure 11c). Such comprehensive structural/tectonic style was observed in the CFTD onshore (Figure 1c; Heilbron et al., 2008; Schmitt et al., 2008). Internally, this heterogeneous SF2/SF3 facies exhibits asymmetric folds with vergence to NW and a

contractional duplex with a possible tectonic transport to NW (Figure 11c). The tectonic transport agrees with kinematic indicators observed onshore in the northern contact zone between the Cabo Frio Tectonic Domain and Oriental Terrane, but not with the indicators from the central and south part of the Domain that verge to E-SE (Schmitt et al., 2016).

The basement samples obtained from wells on the eastern portion of the area (Figure 10a-d) are better correlated with supracrustals units of the CFTD. Lithologically, these predominant biotite gneisses could represent paragneiss from both tectonic domains, since the Oriental Terrane also have high-T paragneisses (Figure 1). The distinction between these paragneisses is given by the contrasting pressure and age during metamorphic peak (ca. 12 Kbar and 520 Ma for CFTD and ca. 5 Kbar and 580 Ma for Oriental Terrane (Egydio-Silva et al., 2018; Heilbron et al., 2008; Schmitt et al., 2016; Schmitt et al., 2018). The geochronological data obtained from the well W-01 ( $533 \pm 15$  Ma) reinforces that this biotite gneiss is better correlated with the Neoproterozoic supracrustal unit of the CFTD. The structural style of this terrane, with exhumed nappes and duplexes of supracrustals unit on top of a homogeneous Paleoproterozoic continental crust (Figure 1c – Schmitt et al., 2016), is also coherent with the overall structural style of the basement in the East Domain, as gentle antiforms of heterogeneous SF3/SF2 over a moderately heterogeneous tabular SF2 (Basal Geobody) and then an homogeneous SF1 basement (Figure 11c). The age is coincident with the metamorphic peak obtained in the Cabo Frio Tectonic Domain (Schmitt et al., 2004, 2016) and also in the Pan African belt in the Angola coast (Monié et al., 2012). In addition, the offshore projection of the Cabo Frio Tectonic Limit (CFTL) is positioned by Egydio-Silva et al. (2018) and Stanton et al. (2019) near the study area following the trend with observed structures onshore (Figure 1a).

We also infer the presence of a high strain, sub-vertical shear zone that coincides approximately with the limit between NE and SE Clusters of intra-basement structures (Figure 11a). Along with the lack of continuity of structures between the clusters (Figure 6c), this limit points divergent dip directions of the basal geobodies, to NW on NE Cluster and to SE in the SE Cluster (Figure 11c). It also coincides with the Central Fault Zone (CFZ) of the rift faults. The segments of the CFZ shows a remarkable straight geometry compared with the others whose anastomosing pattern are predominant. Such geometry is consistent with control given by a single, sub-vertical basement structure. Considering the sub-vertical nature of this shear zone, we are not able to map it in the seismic data. Therefore, this structure might be a subsidiary NE-SW structure, similarly to the shear zones observed in the Oriental Terrane of the Ribeira Belt, parallel to its contact with the CFTD (Figure 1a). Further pre-breakup reconstructions might shed some light in this subject.

## 5.2 | Rift tectonics and models for basement reactivation

The style of rift faults that nucleated from and/or as a result of reactivation of basement shear zones has been discussed in recent studies. While some authors considered the basement shear zones as discrete discontinuities for both analogue models and case studies (e.g. Deng et al., 2018; Vasconcelos et al., 2019, respectively), others take into account not only the geometry but also the 3D shape of shear zones (Collanega et al., 2019; Fazlikhani et al., 2017; Osagiede et al., 2020). Collanega et al. (2019) concluded for the Taranaki Basin (New Zealand) that broader shear zones lead to *en-écheleon* normal fault arrays while narrow shear zones result in continuous faults within the sedimentary cover. It is essential to mention that the Taranaki Basin experienced only an initial rifting deformation and shows a stratigraphically simple and thick (up to 1,800 m) sedimentary filling.

In this study, we used models of basement/rift faults interactions through brittle reactivation proposed to the North Sea Rift by Phillips et al. (2016) and Fazlikhani et al. (2017) as a starting point for the discussion. Both papers considered the angle between basement shear zones and rift-related faults in a profile view as classification criteria, which is a consequence of the angle between the pre-existing intra-basement structures and the extension direction during rifting. Three main schematic models are proposed to explain the interactions between shear zones and rift-related faults, named Merging, Exploitative and Cross-cutting faults (see figure 14 in Phillips et al., 2016). Exploitative rift faults reactivate shear zones parallel to their internal foliation while Merging faults became parallel to the shear zones at depth.

Our seismic interpretation identified examples of these three major types of interactions between intra-basement structures and rift-related faults (Phillips et al., 2016). Exploitative and Merging faults are more abundant than Cross-cutting faults as a consequence of the relatively well oriented (roughly orthogonal) basement grain with respect to the average WNW-ESE extension direction of rift tectonics (Figure 12). The classification used by Phillips et al. (2016) was designed for the wide and discrete Caledonian shear zones bounded by less heterogeneous basement. However, when investigating a more complex basement structure observed in the Neoproterozoic supracrustals of the Cabo Frio Tectonic Domain, some considerations were necessary. Although we have observed a few examples of the Exploitative type in the SE Cluster (Figure 9d), it was not practical to separate the Merging and Exploitative types of interaction. The main reason is the relatively thin sedimentary cover (below the salt) when compared to the area where this classification was initially proposed (Phillips et al., 2016). Thus, both mechanisms mean that to some extent, the exploitation of pre-existing discontinuities occurs through brittle reactivation. For this



reason, we classified the interactions of the basement rift faults as Exploitative and Cross-cutting (Figure 12).

It is evident that the attitudes of rift faults in this study (Figure 5b) might be taken to suggest a persistent WNW-ESE extension direction if we simply consider that the structures are a conjugate set of normal faults with pure dip-slip motion. This extension direction is compatible with the regional extension directions of the Campos Basin (Heine et al., 2013; Savastano et al., 2017). However, under closer scrutiny, by comparing the relative age of fault activity and the syn-kinematic depocentres of Rift Climax(RC) I and RCII sequences (Figures 4c,d, and 5d,e), it is considered more probable that not one, but two distinct extension directions can be interpreted (Figure 13).

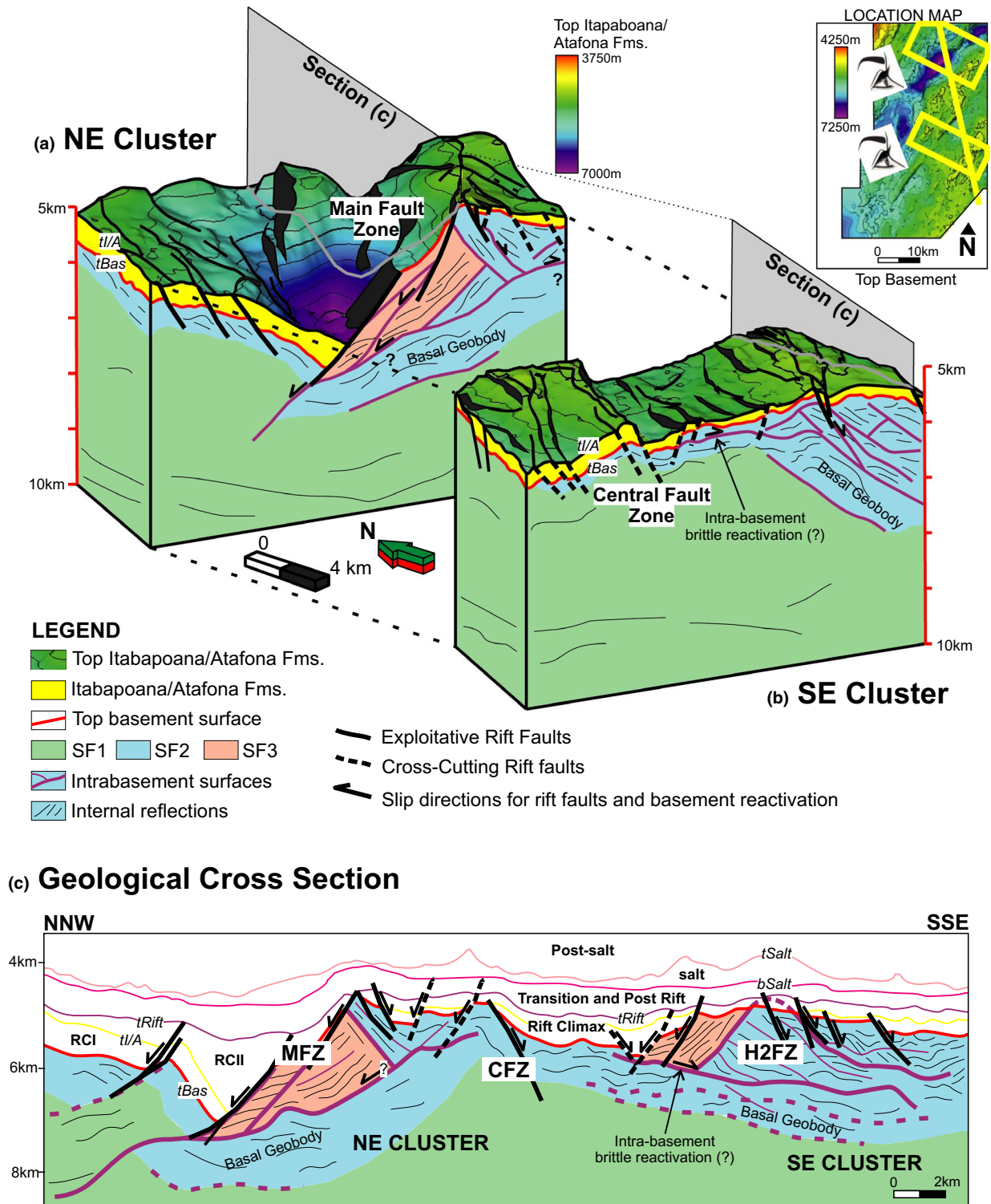
This alternative interpretation of two distinct extension directions should be taken with three further caveats, however. Firstly, some of the faults without syn-kinematic divergent wedges are assigned relative ages of initial activity (propagation to surface) based on the assumption that the fault initiation is marked at the maximum throw horizon. There may be exceptions to this widely used criterion (Walsh & Watterson, 1988), for example, where a basin is substantially underfilled during fault-controlled subsidence (Cartwright, 1991), particularly in structural highs. Secondly, the presence of basement heterogeneities can potentially induce stress perturbations that could lead to faults nucleating oblique to the regional stress field (Collanega et al., 2019; Deng et al., 2018; Osagiede et al., 2020). In fact, this case of sub-parallelism between intra-basement and rift structures is observed in the NE Cluster (compare Figures 7f and h) but not in the SE Cluster (compare Figures 9e and g), where basement and rift structures show the same strike direction. Finally, there are uncertainties in the actual propagation histories of faults that might root at depth into crustal shear zones. For example, the tendency for rift bounding normal faults observed onshore and offshore of Thailand to exhibit low angles shows their ability to reactivate despite being severely misoriented with respect to regional stresses (Morley, 2014). This could be the case of the deeper basement fabric where the MFZ nucleated (Figure 12c). Although these considerations are valid for the East Domain, faults that nucleated in the homogeneous basement of the West Domain (Figure 11a) are unlikely to have been influenced directly in their strike during propagation by basement heterogeneity and thus allow us to make a case for two distinct extension directions based on relative dating.

The relative age of syn-kinematic wedges for faults with contrasting orientation therefore leads us to propose that there was an E-W extension direction operative during the deposition of the RCI sequence that then progressively rotated to a NW-SE direction during RCII. Faults with RCI syn-kinematic wedges show average strike at NNE-SSW while faults with RCII wedges are NE-SW oriented (Figure 13). The spatial distribution of the earlier faults (RCI age), shown in Figure 5d, is uniform within the studied area and, with the exception of the H3FZ, does not include the fault zones of Figure 5c.

Earlier faults can be considered as rift initiation faults, with strain uniformly distributed through growth of generally small-scale faults despite the abundance of intra-basement heterogeneities in the East Domain. Although significant deposition of RCI is observed in some places, the N-S H3FZ shows the most significant wedge-shaped deposits of this age (Figures 4d and 5d), suggesting that this structure nucleated orthogonally to the active extension direction. Less significant RCI depocentres are found on the hanging wall of the Main Fault Zone (MFZ), although it is obliquely oriented to the E-W extension along with intra-basement structures exploited during the nucleation of the MFZ. It is not clear if the central and northern segments of the MFZ were active during RCI since no thickening of RCI sediments is observed on the hanging wall and RCI sediments are absent in the footwall as a result of non-deposition or later erosion.

Later rift faults that nucleated during the deposition of the RCII seismic-sequence mostly occupy the East Domain of the study area (Figure 5e), roughly coinciding with the position of NE and SE Clusters of intra-basement heterogeneities. In addition, Figure 5e shows that most of the fault segments of the MFZ and CFZ, along with significant part of H2FZ, nucleated or have their peak of tectonic activity during the RCII. Faults with syn-kinematic wedges of RCII sediments are NE-SW oriented (Figures 4c and 13b) sustains the interpretation of a NW-SE extension direction during RCII. The strain localization along the fault zones developed during RCII is in accordance with Walsh et al. (1991), where is concluded that as faults grow, many small faults will no longer be required and will become inactive. Later faults are concentrated in the heterogeneous basement in the East Domain, while only a few occurring in the more homogeneous West Domain. From our results, it is suggested that such strain localization could be controlled by intra-basement structures, which could explain the abundance of RCII faults over the East Domain, especially in the SE Cluster (Figures 5e and 13b). Although Walsh et al. (1991) predict that the strain tends to concentrate in few structures during the late rift climax, the abundance of intra-basement structures that were well-oriented to the active extension direction does not follow such a strain evolutionary path.

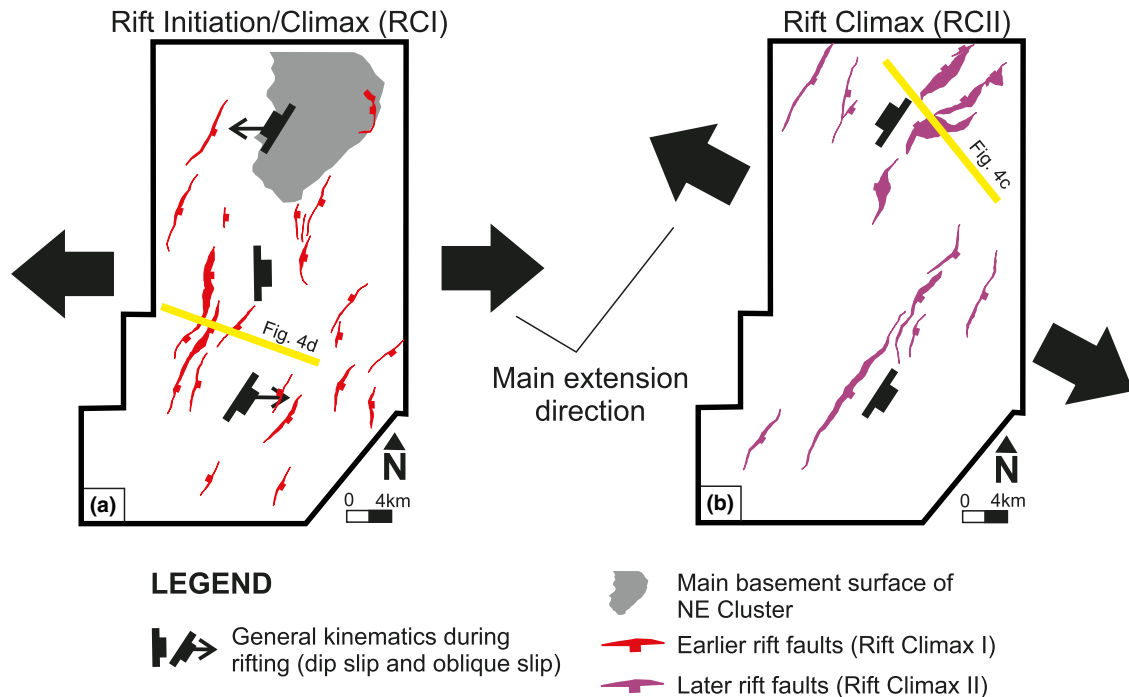
A supplementary control of the strike and dip direction of basement structures on the mode and style of basement reactivations is given by the thickness of heterogeneous basement, expressed by seismic facies (SF2 and SF3) underneath the tBas horizon (Figure 12b,c). Whereas in the North Sea, basement structures are interpreted to occur up to 10 km below the Base Rift horizon (Fazlikhani et al., 2017), in the study area this deeper limit ranges from 4 km below the Top Basement horizon (i.e. up to 8 km depth) to zero (Figures 6b and 12b). This shallower limit of observable basement reflectivity could be simply related to frequency attenuation with depth.



**FIGURE 12** Modes of interaction between intra-basement structures and rift faults in the study area. On the top, (a) and (b) shows a 3D perspective of these interactions for NE and SE intra-basement clusters, respectively. Below, a synthetic geological cross-section (c) across both domains showing the contrasting styles of reactivation between NE and SE clusters. Uninterpreted seismic data is shown on Figure 11b. Slip motions of rift faults and within basement during rifting are shown. MFZ, CFZ, and H2FZ are rift fault zones

However, the transparent seismic response suggests that SF1 below the Basal Geobody in the NE and SE clusters probably represents similar basement geology as in the West Domain. Also, the SF1 occurs at similar depths in the West Domain to

that in which SF2/SF3 are observed in the East Domain, refuting the hypothesis of frequency attenuation. When SF2/SF3 thickness is less than 500 m, Cross-cutting interaction type tends to dominate (Figure 12b). Coincidentally, basement



**FIGURE 13** Interpreted extension directions during the rift initiation and climax tectonic phases, which are equivalent in time with the sediments of the RCI and RCII, respectively. (a) and (b) presents the fault traces that show syn-kinematic wedges (divergent) seismic reflections of, respectively, RCI and RCII sediments in the hanging wall of faults of each age group. Dip direction of normal faults combined with the position of the syn-kinematic depocentres (Figure 5d and e) were used to infer the extension directions for Rift Climax I (a) sequence and Rift Climax II (b) sequence

fabric in the thinner portions of SF2 tends to show a low angle character (the Basal Geobody – Figure 12c), parallel to the predicted extension direction (Figure 13), so a Cross-cutting interaction is more likely to have occurred.

### 5.3 | Basement reactivations within the NE cluster

We observed that central and northern segments of the Main Fault Zone (MFZ) have an abnormal dip (low angle) and strike attributes (Figure 8e) when compared to the remaining mapped rift faults as a whole (Figure 5b). The MFZ is deeply rooted, merging with a low angle ( $<25^\circ$ ) highly heterogeneous basement fabric, mostly constituted of SF3 (Figure 12a). The combination of MFZ attributes (Figure 8) such as obliquity with respect to the main conjugate pair of rift faults (Figure 5b) and the coeval deposition of thick syn-kinematic wedges of RCII sediments (Figure 4c) suggests that MFZ nucleates as a consequence of basement reactivation during the rift climax stage. Although it is clear that the peak of MFZ fault activity was during RCII, we cannot distinguish whether the fault was nucleated during the Rift Initiation (RCI) or RCII stage. For that, a study considering the E-W extension during RCI and the orientation of intra-basement structures

beneath the MFZ could potentially test the possibility that the basement fabric would be reactivated under a E-W extension. The NE-SW strike, NW dipping low angle basement shear zones could have been obliquely reactivated during Rift Climax I (RCI) by E-W extension. The extensional component was meaningful, leading to deposition of significant RCI layers in the hanging wall (Figure 5d). However, there are no RCI sediments in the footwall of the MFZ and no fault-related syn-kinematic wedges of RCI sediments in the hanging wall. Later, the extension direction progressively rotated clockwise to NW-SE strike, therefore inducing dip-slip kinematics on the MFZ and accumulation of the thickest depocentres of RCII deposits in its hanging wall (Figure 5e).

The N-S oriented H3FZ and the southern segments of the MFZ have a slightly different evolution compared to its main sector. We suggest that the nucleation of the N-S structures was not triggered by reactivation of basement structures during rift initiation. The relative absence of basement heterogeneities in the expense of a more isotropic basement on W-34 nearby (Figure 10e) means that there are fewer structures upon which strain can localize, so faults nucleated regardless pre-existing discontinuities. From this, two possible interpretations are possible: (a) The nucleation of the H3FZ and southern segments of MFZ was concomitant with the onset of the oblique reactivation of basement structures on



the NE-SW main segments of the MFZ during RCI. These segments eventually linked and later the H3FZ and the southern segments of MFZ became inactive while the main branch of MFZ kept evolving during the RCII as a consequence of the progressive clockwise rotation of the extension direction from E-W to NW-SE (Figure 13). (b) The H3FZ and the southern segments of MFZ evolved as an isolated graben during RCI. Then the main NE-SW segments of the MFZ nucleated during RCII and thus linked southwards with the pre-existing N-S faults of the H3FZ and the southern tip of the MFZ. Either hypothesis explains the diachronous sedimentation of RCI and RCII sequences along the hanging wall of the MFZ (Figure 4b). A definitive answer would require detailed tectonostratigraphic and kinematic analysis, which is beyond the scope of this paper.

Recently, high-resolution Discrete Element Modelling (DEM) have been used to simulate the effects of pre-existing basement discontinuities on the onset and geometry of rift-related faults. Deng et al. (2018) built a DEM including a pre-existing basement discontinuity with constant area and dip angle, overlain by a 6 km thick sedimentary column, but changing its strike direction in order to create four scenarios of obliquity between basement structure and extension direction. Apart from the oversimplified basement heterogeneities and thicker sedimentary section compared to our study area, the resultant geometry from the model using a 60° angle between the maximum extension direction and the orientation of pre-existing basement weaknesses is similar to the MFZ. Here, we observed an average obliquity of 15° (i.e. 75° relative to the assumed main extension) with respect to the main strike of the normal faults. This finding reinforces the development of non-collinear rift faults as a consequence of stress-field perturbations induced by broad basement shear zones, such as the results obtained from 3D seismic data by Osagiede et al. (2020). Our interpretation is that the subtle oblique character of the shallower segments compared to the deepest sectors of MFZ along with the overall sub-parallelism between intra-basement and rift structures in the NE cluster (Figure 7f,g, respectively) are the consequence of stress-field perturbations propagated upwards through the sedimentary column during RCII.

A more localized, selective reactivation of basement structures is observed on the footwall block of the MFZ. The basement here comprises the eastern limb of the anti-form, which merges with the basal geobody towards the east (Figures 7d and 12c). We suggest that rift faults in this position have shorter lengths and smaller displacements because of a combination of three factors: (a) the MFZ focused the strain in this region, in accordance with Walsh et al. (1991); (b) basement heterogeneities are less continuous and do not exhibit a persistent orientation when compared to the basement fabric near the MFZ; (c) heterogeneous basement (SF2/SF3) is progressively shallower eastwards and its internal anisotropies (Basal Geobody) are usually oriented at

a high angle to rift faults (east of Figure 12a). This leads to cross-cutting fault-basement relationships rather than exploitative relationships (Phillips et al., 2016).

## 5.4 | Basement reactivations within the SE cluster

Reactivations of basement shear zones during rifting in the SE Cluster shows a substantial difference in style and mechanisms when compared to the NE Cluster (Figure 12). In the NE Cluster, the MFZ localized most of the strain, whereas in the SE Cluster faulting is distributed along several small displacement faults (Figures 5 and 12). Our interpretation for the contrasting styles of basement reactivations within the SE Cluster is that basement structures within this area are more abundant and is consisted of smaller intra-basement structures in terms of length/area than those in the NE cluster (compare Figures 7b, 9b and 12c). This means a more diffuse strain distribution, where many intra-basement surfaces were continuously reactivated during both the Rift Climax I and II stages thus accommodating minor displacements. Strain hardening of the fault planes in early rift faults combined with the number of pre-existing intra-basement structures well-oriented to the rift extension that are prone to be reactivated are the most likely explanation for strain distribution in the SE Cluster. This interpretation is supported by noticeable parallelism in strike between intra-basement structures and rift faults, observed both in stereograms (Figure 9e,g) and time-slice interpretations (Figure 9b,c). In addition, the lower dip angle of basement surfaces combined with the parallelism in strike with rift faults agrees with fault-merge and fault exploiting mechanisms (Phillips et al., 2016) as the predominant basement-rift faults interactions (Figure 12b). A similar exploitation mechanism is suggested where the intra-basement structure exhibits an antiform geometry, thus controlling rift faults with dips conformable to the fold limbs (Figure 12c). Finally, the Cross-Cut basement-rift faults interaction type predominates where basement heterogeneities are thinner underneath the tBas (basal geobody) and exhibit a predominantly high angle with the rift faults (Figure 12b,c). This geometric relationship makes it very difficult for basement structures to be reactivated during the extension such that rift faults nucleates at a high angle with respect to basement anisotropy.

A potential additional mechanism of strain distribution throughout basement heterogeneities during rifting is low angle shear zone reactivation, similar to the outcomes of Fossen et al. (2017). They used macro and micro-structural analysis in outcrops supported by geochronological data to evidence brittle reactivations as shear fractures along low to very low-angle (ca. 5°) Caledonian basal thrust or décollements on onshore Norway. This type of movement

is exclusively intra-basement reactivation and therefore not obvious on seismic data due to the lack of seismic kinematic markers within the basement. An example of such mechanism is observed on the transition between the NE and SE clusters in Figure 12c. Heterogeneous SF3 and merging rift faults interact with a shallow Basal Geobody at a right angle, on which top we assume low angle reactivation. A similar mechanism might also be present within the basement adjacent to the MFZ (Figure 12).

## 6 | CONCLUSIONS

1. 3D seismic facies interpretation of intra-basement reflections leads to the identification of two contrasting basement domains. The East Domain is heterogeneous and is equivalent to the supracrustals of the Cabo Frio Tectonic Domain (CFTD). The West Domain is homogenous and could represent either the Paleoproterozoic basement of the CFTD or the Oriental Terrane of the Ribeira Belt.
2. The rift faults developed from Hauterivian to Barremian as a result of a progressive rotation of extension from E-W to NW-SE, resulting in two fault sets with distinct episodes of deposition of syn-kinematic wedges. Such episodes are approximately equivalent to the rift initiation and rift climax tectonic stages.
3. The rift tectonics took advantage of a well-oriented basement structure, roughly orthogonal to the extension direction, resulting in a dominance of exploitative brittle reactivation of basement structures during rifting.
4. Contrasting basement heterogeneity between the East and West Domains controlled the strain distribution during rift-related faulting. In the heterogeneous East Domain, the pre-existing fabric was selective reactivated whenever the orientation was favourable, resulting in faults forming progressively as the extension direction rotates. Where the basement is homogeneous (West Domain), early formed faults tend to dominate throughout the rifting.

## ACKNOWLEDGEMENTS

The results and interpretations of this paper are part of the DPhil research project of MS, funded by Petróleo Brasileiro S.A. – Petrobras. The authors thank Petrobras, for supporting this study and for the opportunity to publish this paper. Fernando Jardim, Leonardo Onofre and Otávio Lima from Petrobras are thanked for the support on data loading and constructive feedback during the interpretation. We acknowledge Schlumberger for provision of the seismic interpretation software used. Renata da Silva Schmitt thanks CNPq research grant 311748/2018-0 and to the Gondwana Map Project (CENPES-UFRJ- 13850). This paper is a contribution to IGCP-628 “The Geological Map and Tectonic evolution of Gondwana”. The Editor-in-Chief Atle Rotevatn

and the three reviewers, Hamed Fazlikhani, Thomas Phillips and Christopher Sæbø Serck are thanked for their constructive and detailed comments which improved the manuscript significantly. We wish to thank Christopher Kirkham for the final review of the manuscript.

## CONFLICT OF INTEREST

The authors have no conflict of interest to declare.

## PEER REVIEW

The peer review history for this article is available at <https://publons.com/publon/10.1111/bre.12540>.

## ORCID

Michael Strugale  <https://orcid.org/0000-0003-1106-7529>

Renata da Silva Schmitt  <https://orcid.org/0000-0001-6349-5459>

Joe Cartwright  <https://orcid.org/0000-0003-4198-9719>

## REFERENCES

- Alkmim, F. F., Marshak, S., Pedrosa-Soares, A. C., Peres, G. G., Cruz, S. C. P., & Whittington, A. (2006). Kinematic evolution of the Araçuaí-West Congo orogen in Brazil and Africa: Nutcracker tectonics during the Neoproterozoic assembly of Gondwana. *Precambrian Research*, 149, 43–64. <https://doi.org/10.1016/j.precamres.2006.06.007>
- Almeida, F. F. M., Hasui, Y., Brito Neves, B. B., & Fuck, R. A. (1981). Brazilian structural provinces: An introduction. *Earth-Science Reviews*, 17, 1–29. [https://doi.org/10.1016/0012-8252\(81\)90003-9](https://doi.org/10.1016/0012-8252(81)90003-9)
- Almeida, J. C. H., Tupinambá, M., Heilbron, M., & Trouw, R. A. J. (1998). Geometric and kinematic analysis at the Central Tectonic Boundary of the Ribeira belt, Southeastern Brazil. Congresso Brasileiro de Geologia, 40, Belo Horizonte, Sociedade Brasileira de Geologia.
- Bertani, R. T., & Carozzi, A. V. (1985a). Lagoa Feia Formation (Lower Cretaceous) Campos Basin, offshore Brazil: Rift valley type lacustrine carbonate reservoirs—II. *Journal of Petroleum Geology*, 8, 199–220. <https://doi.org/10.1111/j.1747-5457.1985.tb01011.x>
- Bertani, R. T., & Carozzi, A. V. (1985b). Lagoa Feia Formation (Lower Cretaceous) Campos Basin, offshore Brazil: Rift valley type lacustrine carbonate reservoirs - I. *Journal of Petroleum Geology*, 8, 37–58. <https://doi.org/10.1111/j.1747-5457.1985.tb00190.x>
- Bird, P. C., Cartwright, J. A., & Davies, T. L. (2014). Basement reactivation in the development of rift basins: An example of reactivated Caledonide structures in the West Orkney Basin. *Journal of the Geological Society*, 172, 77–85. <https://doi.org/10.1144/jgs2013-098>
- Brito Neves, B. B., Campos Neto, M. C., & Fuck, R. A. (1999). From Rodinia to Western Gondwana: An approach to the Brasiliano-Pan African Cycle and orogenic collage. *Episodes*, 22, 155–166. <https://doi.org/10.18814/epiiugs/1999/v22i3/002>
- Bühn, B., Pimentel, M. M., Matteini, M., & Dantas, E. L. (2009). High spatial resolution analysis of Pb and U isotopes for geochronology by laser ablation multi-collector inductively coupled plasma mass spectrometry (LA-MC-ICP-MS). *Anais Da Academia Brasileira De Ciências*, 81, 99–114. <https://doi.org/10.1590/S0001-37652009001000011>
- Cainelli, C., & Mohriak, W. U. (1999). Some remarks on the evolution of sedimentary basins along the Eastern Brazilian continental

- margin. *Episodes*, 22, 206–216. <https://doi.org/10.18814/epiug/1999/v22i3/008>
- Calegari, S. S., Neves, M. A., Guadagnin, F., França, G. S., & Vincentelli, M. G. C. (2016). The Alegre Lineament and its role over the tectonic evolution of the Campos Basin and adjacent continental margin, Southeastern Brazil. *Journal of South American Earth Sciences*, 69, 226–242. <https://doi.org/10.1016/j.jsames.2016.04.005>
- Carmo, I., Schmitt, R., Araújo, M., & Romeiro, M. (2017). Evidence for the Paleoproterozoic/Cambrian Angolan belt in the Brazilian margins—new data from offshore basement drill core. Porto de -5th Conjugate Margins Conference, Porto de Galinhas – Brazil.
- Cartwright, J. (1991). The kinematic evolution of the Coffee Soil Fault. *Geological Society, London, Special Publications*, 56, 29–40. <https://doi.org/10.1144/GSL.SP.1991.056.01.03>
- Cartwright, J., Bouroullac, R., James, D., & Johnson, H. (1998). Polycyclic motion history of some Gulf Coast growth faults from high-resolution displacement analysis. *Geology*, 26, 819–822. [https://doi.org/10.1130/0091-7613\(1998\)026%3C0819:PMHOSG%3E2.3.CO;2](https://doi.org/10.1130/0091-7613(1998)026%3C0819:PMHOSG%3E2.3.CO;2)
- Cavalcante, C., Fossen, H., de Almeida, R. P., Hollanda, M. H. B. M., & Egydio-Silva, M. (2019). Reviewing the puzzling intracontinental termination of the Araçuaí-West Congo orogenic belt and its implications for orogenic development. *Precambrian Research*, 322, 85–98. <https://doi.org/10.1016/j.precamres.2018.12.025>
- Chang, H. K., Kowsmann, R. O., Figueiredo, A. M. F., & Bender, A. A. (1992). Tectonics and stratigraphy of the East Brazil Rift system: An overview. *Tectonophysics*, 213, 97–138. [https://doi.org/10.1016/0040-1951\(92\)90253-3](https://doi.org/10.1016/0040-1951(92)90253-3)
- Childs, C., Manzocchi, T., Walsh, J. J., Bonson, C. G., Nicol, A., & Schöpfer, M. P. (2009). A geometric model of fault zone and fault rock thickness variations. *Journal of Structural Geology*, 31, 117–127. <https://doi.org/10.1016/j.jsg.2008.08.009>
- Collanega, L., Siuda, K., Jackson, C.-A.-L., Bell, R. E., Coleman, A. J., Lenhart, A., Magee, C., & Breda, A. (2019). Normal fault growth influenced by basement fabrics: The importance of preferential nucleation from pre-existing structures. *Basin Research*, 31, 659–687. <https://doi.org/10.1111/bre.12327>
- Daly, M. C., Chorowicz, J., & Fairhead, J. D. (1989). Rift basin evolution in Africa: The influence of reactivated steep basement shear zones. *Geological Society, London, Special Publications*, 44, 309–334. <https://doi.org/10.1144/GSL.SP.1989.044.01.17>
- Dehler, N. M., Magnavita, L. P., Gomes, L. C., Rigoti, C. A., de Oliveira, J. A. B., Sant'Anna, M. V., & Costa, F. G. D. (2016). The 'Helmut' geophysical anomaly: A regional left-lateral transtensional shear zone system connecting Santos and Campos Basins, southeastern Brazil. *Marine and Petroleum Geology*, 72, 412–422. <https://doi.org/10.1016/j.marpetgeo.2016.01.012>
- Deng, C., Gawthorpe, R. L., Fossen, H., & Finch, E. (2018). How does the orientation of a preexisting basement weakness influence fault development during renewed rifting? Insights from three-dimensional discrete element modeling. *Tectonics*, 37, 2221–2242. <https://doi.org/10.1029/2017TC004776>
- Dias, J. L., Oliveira, J. Q., & Vieira, J. C. (1988). Sedimentological and stratigraphic analysis of the Lagoa Feia formation, rift phase of Campos Basin, Offshore Brazil. *Brazilian Journal of Geology*, 18, 252–260. <https://doi.org/10.25249/0375-7536.1988252260>
- Ebert, H. D., & Hasui, Y. (1998). Transpressional tectonics and strain partitioning during oblique collision between three plates in the Precambrian of southeast Brazil. *Geological Society, London, Special Publications*, 135, 231–252. <https://doi.org/10.1144/GSL.SP.1998.135.01.15>
- Egydio-Silva, M., Vauchez, A., Fossen, H., Cavalcante, G. C. G., & Xavier, B. C. (2018). Connecting the Araçuaí and Ribeira belts (SE-Brazil): Progressive transition from contractional to transpressive strain regime during the Brasiliano orogeny. *Journal of South American Earth Sciences*, 86, 127–139. <https://doi.org/10.1016/j.jsames.2018.06.005>
- Fazlikhani, H., Fossen, H., Gawthorpe, R. L., Faleide, J. I., & Bell, R. E. (2017). Basement structure and its influence on the structural configuration of the northern North Sea rift. *Tectonics*, 36, 1151–1177. <https://doi.org/10.1002/2017TC004514>
- Fetter, M. (2009). The role of basement tectonic reactivation on the structural evolution of Campos Basin, offshore Brazil: Evidence from 3D seismic analysis and section restoration. *Marine and Petroleum Geology*, 26, 873–886. <https://doi.org/10.1016/j.marpetgeo.2008.06.005>
- Fossen, H., Khani, H. F., Faleide, J. I., Ksienzyk, A. K., & Dunlap, W. J. (2017). Post-Caledonian extension in the West Norway–northern North Sea region: The role of structural inheritance. *Geological Society, London, Special Publications*, 439, 465–486. <https://doi.org/10.1144/SP439.6>
- Guardado, L. R., Gamboa, L. A. P., & Lucchesi, C. F. (1989). Petroleum Geology of the Campos Basin, Brazil, a Model for a producing atlantic type basin: part 2. In J. D. Edwards & P. A. Santogrossi (Eds.), *Memoir* (Vol. 48, pp. 37–79). AAPG.
- Heilbron, M., Valeriano, C. M., Tassinari, C. C. G., Almeida, J., Tupinambá, M., Siga, O., & Trouw, R. (2008). Correlation of Neoproterozoic terranes between the Ribeira Belt, SE Brazil and its African counterpart: Comparative tectonic evolution and open questions. *Geological Society, London, Special Publications*, 294, 211–237. <https://doi.org/10.1144/SP294.12>
- Heine, C., Zoethout, J., & Müller, R. D. (2013). Kinematics of the South Atlantic rift. *Solid Earth*, 4, 215–253. <https://doi.org/10.5194/se-4-215-2013>
- Herlinger, R. Jr, Zambonato, E. E., & De Ros, L. F. (2017). Influence of diagenesis on the quality of lower cretaceous pre-salt lacustrine carbonate reservoirs from northern Campos Basin, offshore Brazil. *Journal of Sedimentary Research*, 87, 1285–1313. <https://doi.org/10.2110/jsr.2017.70>
- Kallweit, R., & Wood, L. (1982). The limits of resolution of zero-phase wavelets. *Geophysics*, 47, 1035–1046. <https://doi.org/10.1190/1.1441367>
- Lenhart, A., Jackson, C.-A.-L., Bell, R. E., Duffy, O. B., Gawthorpe, R. L., & Fossen, H. (2019). Structural architecture and composition of crystalline basement offshore west Norway. *Lithosphere*, 11, 273–293. <https://doi.org/10.1130/L668.1>
- Lima, B. E. M., & De Ros, L. F. (2019). Deposition, diagenetic and hydrothermal processes in the Aptian Pre-Salt lacustrine carbonate reservoirs of the northern Campos Basin, offshore Brazil. *Sedimentary Geology*, 383, 55–81. <https://doi.org/10.1016/j.sedgeo.2019.01.006>
- Lima, B. E. M., Tedeschi, L. R., Pestilho, A. L. S., Santos, R. V., Vazquez, J. C., Guzzo, J. V. P., & De Ros, L. F. (2020). Deep-burial hydrothermal alteration of the Pre-Salt carbonate reservoirs from northern Campos Basin, offshore Brazil: Evidence from petrography, fluid inclusions. *Sr, C and O Isotopes*, 113, 104–143. <https://doi.org/10.1016/j.marpetgeo.2019.104143>
- Ludwig, K. R. (2003). User's manual for isoplot 3.00, a geochronological toolkit for microsoft excel. *Berkeley Geochronology Center Special Publications*, 4, 25–32.
- Milani, E. J., & Davison, I. (1988). Basement control and transfer tectonics in the Recôncavo-Tucano-Jatobá rift, Northeast Brazil. *Tectonophysics*, 154, 41–70. [https://doi.org/10.1016/0040-1951\(88\)90227-2](https://doi.org/10.1016/0040-1951(88)90227-2)



- Mitchum, R. M. Jr, Vail, P. R., & Thompson, S. III (1977). Seismic stratigraphy and global changes of sea level: Part 2. The depositional sequence as a basic unit for stratigraphic analysis: Section 2. Application of seismic reflection configuration to stratigraphic interpretation. *AAPG Memoir*, 26, 53–62.
- Mizuno, T. A., Mizusaki, A. M. P., & Lykawka, R. (2018). Facies and paleoenvironments of the Coqueiros Formation (Lower Cretaceous, Campos Basin): A high frequency stratigraphic model to support pre-salt “coquinas” reservoir development in the Brazilian continental margin. *Journal of South American Earth Sciences*, 88, 107–117. <https://doi.org/10.1016/j.jsames.2018.07.007>
- Mizusaki, A. M. P., Petrini, R., Bellieni, P., Comin-Chiaramonti, P., Dias, J., De Min, A., & Piccirillo, E. M. (1992). Basalt magmatism along the passive continental margin of SE Brazil (Campos Basin). *Contributions to Mineralogy and Petrology*, 111, 143–160. <https://doi.org/10.1007/BF00348948>
- Monié, P., Bosch, D., Bruguier, O., Vauchez, A., Rolland, Y., Nsungani, P., & Buta Neto, A. (2012). The Late Neoproterozoic/Early Palaeozoic evolution of the West Congo Belt of NW Angola: Geochronological (U-Pb and Ar-Ar) and petrostructural constraints. *Terra Nova*, 24, 238–247. <https://doi.org/10.1111/j.1365-3121.2012.01060.x>
- Morley, C. K. (2014). The widespread occurrence of low-angle normal faults in a rift setting: Review of examples from Thailand, and implications for their origin and evolution. *Earth Science Reviews*, 133, 18–42. <https://doi.org/10.1016/j.earscirev.2014.02.007>
- Morley, C. K., Haranya, C., Phoosongsee, W., Pongwapee, S., Kornsawan, A., & Wonganan, N. (2004). Activation of rift oblique and rift parallel pre-existing fabrics during extension and their effect on deformation style: Examples from the rifts of Thailand. *Journal of Structural Geology*, 26, 1803–1829. <https://doi.org/10.1016/j.jsg.2004.02.014>
- Moulin, M., Aslanian, D., & Unternehr, P. (2010). A new starting point for the South and Equatorial Atlantic Ocean. *Earth-Science Reviews*, 98, 1–37. <https://doi.org/10.1016/j.earscirev.2009.08.001>
- Muniz, M. C., & Bosence, D. W. J. (2015). Pre-salt microbialites from the Campos Basin (offshore Brazil): Image log facies, facies model and cyclicity in lacustrine carbonates. *Geological Society, London, Special Publications*, 418, 221–242. <https://doi.org/10.1144/SP418.10>
- Olivito, J. P. R., & Souza, F. J. (2020). Depositional model of early Cretaceous lacustrine carbonate reservoirs of the Coqueiros formation-Northern Campos Basin, southeastern Brazil. *Marine and Petroleum Geology*, 111, 414–439. <https://doi.org/10.1016/j.marpetgeo.2019.07.013>
- Osagiede, E. E., Rotevatn, A., Gawthorpe, R., Kristensen, T. B., Jackson, C.-A.-L., & Marsh, N. (2020). Pre-existing intra-basement shear zones influence growth and geometry of non-colinear normal faults, western Utsira High-Heimdal Terrace, North Sea. *Journal of Structural Geology*, 130, 103908. <https://doi.org/10.1016/j.jsg.2019.103908>
- Peacock, D., Knipe, R., & Sanderson, D. (2000). Glossary of normal faults. *Journal of Structural Geology*, 22, 291–305. [https://doi.org/10.1016/S0191-8141\(00\)80102-9](https://doi.org/10.1016/S0191-8141(00)80102-9)
- Phillips, T. B., Jackson, C.-A.-L., Bell, R. E., Duffy, O. B., & Fossen, H. (2016). Reactivation of intrabasement structures during rifting: A case study from offshore southern Norway. *Journal of Structural Geology*, 91, 54–73. <https://doi.org/10.1016/j.jsg.2016.08.008>
- Prosser, S. (1993). Rift-related linked depositional systems and their seismic expression. *Geological Society, London, Special Publications*, 71, 35–66. <https://doi.org/10.1144/GSL.SP.1993.071.01.03>
- Reeve, M. T., Bell, R. E., Duffy, O. B., Jackson, C.-A.-L., & Sansom, E. (2015). The growth of non-colinear normal fault systems; What can we learn from 3D seismic reflection data? *Journal of Structural Geology*, 70, 141–155. <https://doi.org/10.1016/j.jsg.2014.11.007>
- Reeve, M. T., Bell, R. E., & Jackson, C.-A.-L. (2014). Origin and significance of intra-basement seismic reflections offshore western Norway. *Journal of the Geological Society*, 171, 1–4. <https://doi.org/10.1144/jgs2013-020>
- Savastano, V. L. M., Schmitt, R. S., Araújo, M. N. C., & Inocêncio, L. C. (2017). Rift brittle deformation of SE-Brazilian continental margin: Kinematic analysis of onshore structures relative to the transfer and accommodation zones of southern Campos Basin. *Journal of Structural Geology*, 94, 136–153. <https://doi.org/10.1016/j.jsg.2016.11.012>
- Schmitt, R. S., Fragoso, R. A., & Collins, A. S. (2018). Suturing Gondwana in the Cambrian: The Orogenic Events of the Final Amalgamation. In S. Siegesmund, M. A. S. Basei, P. Oyhançabal, & S. Oriolo (Eds.), *Geology of Southwest Gondwana* (pp. 411–432). Springer International Publishing.
- Schmitt, R. S., Trouw, R., Van Schmus, W. R., Armstrong, R., & Stanton, N. S. G. (2016). The tectonic significance of the Cabo Frio Tectonic Domain in the SE Brazilian margin: A Paleoproterozoic through Cretaceous saga of a reworked continental margin. *Brazilian Journal of Geology*, 46, 37–66. <https://doi.org/10.1590/2317-4892.01620150025>
- Schmitt, R. S., Trouw, R. A. J., Van Schmus, W. R., & Passchier, C. W. (2008). Cambrian orogeny in the Ribeira Belt (SE Brazil) and correlations within West Gondwana: Ties that bind underwater. *Geological Society, London, Special Publications*, 294, 279–296. <https://doi.org/10.1144/SP294.15>
- Schmitt, R. S., Trouw, R. A. J., Van Schmus, W. R., & Pimentel, M. M. (2004). Late amalgamation in the central part of West Gondwana: New geochronological data and the characterization of a Cambrian collisional orogeny in the Ribeira Belt (SE Brazil). *Precambrian Research*, 133, 29–61. <https://doi.org/10.1016/j.precamres.2004.03.010>
- Silva, M. A., Camozzato, E., Paes, V. J. C., Junqueira, P. A., & Ramgrab, G. E. (2004). Carta Geológica do Brasil ao Milionésimo, Folha SF. 24-Vitoria. CPRM. Brasília. [http://rigeo.cprm.gov.br/xmlui/bitstream/handle/doc/4998/sf24\\_Vitoria.pdf](http://rigeo.cprm.gov.br/xmlui/bitstream/handle/doc/4998/sf24_Vitoria.pdf)
- Stanton, N., Kuszniir, N., Gordon, A., & Schmitt, R. S. (2019). Architecture and Tectono-magmatic evolution of the Campos Rifted Margin: Control of OCT structure by basement inheritance. *Marine and Petroleum Geology*, 100, 43–59. <https://doi.org/10.1016/j.marpetgeo.2018.10.043>
- Stanton, N., Schmitt, R. S., Galdeano, A., Maia, M., & Mane, M. (2010). Crustal structure of the southeastern Brazilian margin, Campos Basin, from aeromagnetic data: New kinematic constraints. *Tectonophysics*, 490, 15–27. <https://doi.org/10.1016/j.tecto.2010.04.008>
- Szatmari, P., & Milani, E. J. (2016). Tectonic control of the oil-rich large igneous-carbonate-salt province of the South Atlantic rift. *Marine and Petroleum Geology*, 77, 567–596. <https://doi.org/10.1016/j.marpetgeo.2016.06.004>
- Thompson, D. L., Stilwell, J. D., & Hall, M. (2015). Lacustrine carbonate reservoirs from Early Cretaceous rift lakes of Western Gondwana: Pre-salt coquinas of Brazil and West Africa. *Gondwana Research*, 28, 26–51. <https://doi.org/10.1016/j.gr.2014.12.005>
- Torsvik, T. H., Rouse, S., Labails, C., & Smethurst, M. A. (2009). A new scheme for the opening of the South Atlantic Ocean and the dissection

- of an Aptian salt basin. *Geophysical Journal International*, 177, 1315–1333. <https://doi.org/10.1111/j.1365-246X.2009.04137.x>
- Vasconcelos, D. L., Bezerra, F. H., Medeiros, W. E., de Castro, D. L., Clausen, O. R., Vital, H., & Oliveira, R. G. (2019). Basement fabric controls rift nucleation and postrift basin inversion in the continental margin of NE Brazil. *Tectonophysics*, 751, 23–40. <https://doi.org/10.1016/j.tecto.2018.12.019>
- Walsh, J. J., & Watterson, J. (1988). Analysis of the relationship between displacements and dimensions of faults. *Journal of Structural Geology*, 10, 239–247. [https://doi.org/10.1016/0191-8141\(88\)90057-0](https://doi.org/10.1016/0191-8141(88)90057-0)
- Walsh, J., Watterson, J., & Yielding, G. (1991). The importance of small-scale faulting in regional extension. *Nature*, 351, 391–393. <https://doi.org/10.1038/351391a0>
- Winter, W. R., Jahnert, R. J., & França, A. B. (2007). Bacia de campos. *Boletim De Geociências Da Petrobras*, 15, 511–529.
- Withjack, M. O., Schlische, R. W., & Olsen, P. E. (1998). Diachronous rifting, drifting, and inversion on the passive margin of central eastern North America: An analog for other passive margins. *AAPG Bulletin*, 82, 817–835. <https://doi.org/10.1306/1D9BC60B-172D-11D7-8645000102C1865D>
- Wright, V. P., & Barnett, A. J. (2015). An abiogenic model for the development of textures in some South Atlantic early Cretaceous lacustrine carbonates. *Geological Society, London, Special Publications*, 418(1), 209–219. <https://doi.org/10.1144/SP418.3>

**How to cite this article:** Strugale M, Schmitt R S, Cartwright J. Basement geology and its controls on the nucleation and growth of rift faults in the northern Campos Basin, offshore Brazil. *Basin Res.* 2021;33:1906–1933. <https://doi.org/10.1111/bre.12540>